Assessing multi-hazard susceptibility to cryospheric hazards: lesson learnt from an Alaskan example

Letizia Elia[1*], Silvia Castellaro[1], Ashok Dahal[2], Luigi Lombardo[2]

Abstract

Classifying a given landscape on the basis of its susceptibility to surface processes is a standard procedure in low to mid-latitudes. Conversely, these procedures have hardly been explored in periglacial regions, primarily because of the limited presence of human settlements and, therefore, the little need for risk assessment. However, global warming is radically changing this situation and will change it even more in the future. For this reason, understanding the spatial and spatiotemporal dynamics of geomorphological processes in peri-arctic environments can be crucial to make informed decisions in such unstable environments and shed light on what changes may follow at lower latitudes. For this reason, here we explored the use of data-driven models capable of recognizing locations prone to develop retrogressive thaw slumps (RTSs) and/or active layer detachments (ALDs). These are cryospheric hazards induced by permafrost degradation, and their development can negatively affect human settlements or infrastructure, change the sediment budget dynamics and release greenhouse gases. Specifically, we test a binomial Generalized Additive Modeling structure to estimate the probability of RST and ALD occurrences in the North sector of the Alaskan territory. The results we obtain show that our binary classifiers can accurately recognize locations prone to RTS and ALD, in a number of goodness-of-fit ($\mathrm{AUC_{RTS}} = 0.83$; $\mathrm{AUC_{ALD}} = 0.86$), random cross-validation (mean $\mathrm{AUC_{RTS}} = 0.82$; mean $\mathrm{AUC_{ALD}} = 0.86$), and spatial cross-validation (mean $\mathrm{AUC_{RTS}} = 0.74$; mean $\mathrm{AUC_{ALD}} = 0.80$) routines. Overall, our analytical protocol has been implemented to build an open-source tool scripted in Python as part of an interactive Jupyter notebook where all the operational steps are automatized for anyone to replicate the same experiment. Our protocol allows one to access cloud-stored information, pre-process it, and download it locally to be integrated for spatial predictive purposes.

Data and codes can be accessed at this GitHub repository: CryoS.

Keywords: Spatial modeling; retrogressive thaw slides; open source scripting; susceptibility assessment; cryospheric hazards.

[1]Department of Physics and Astronomy, Alma Mater Studiorum University of Bologna, Viale Berti Pichat 6/2, 40127 Bologna, Italy

[2]University of Twente, Faculty of Geo-Information Science and Earth Observation (ITC), PO Box 217, Enschede, AE 7500, Netherlands

1 Introduction

Techniques aimed at estimating locations prone to hydro-geomorphic hazards have seen significant development since the inception of the susceptibility concept. In its most modern definition, susceptibility refers to the probability of a given process occurring at a certain location (Reichenbach et al., 2018). This definition has been applied in studying a number of geomorphological processes, spanning from landslides (Atkinson and Massari, 1998; Frattini et al., 2010), to water-based (Conforti et al., 2011; Titti et al., 2022a) and wind-based (Borrelli et al., 2014, 2016) soil erosion, floods (Choubin et al., 2019; Wang et al., 2022a) and more. A similar progress has characterized modeling each of these phenomena, starting from expert-based mapping solutions (Brabb et al., 1972; Verstappen, 1983) where geoscientists recognized susceptible areas on the basis of their experience. In a second step, with the advent of Geographic Information Systems (Longley et al., 2005), more numerically-oriented solutions were proposed, starting from heuristic weighting (Leoni et al., 2009) to a number of bivariate statistical tools such as certainty factors (Juliev et al., 2019), weight of evidence (Regmi et al., 2010), etc. However, these tools all suffered from the same flaw, being unable to provide rigorous probabilistic outputs (Lombardo and Mai, 2018). This is the reason why most of the geoscientific community welcomed multivariate statistics, largely in the form of simplistic Generalized Linear Models (Atkinson and Massari, 1998; Quesada-Román et al., 2019) In a subsequent phase, machine learning tools have then occupied the majority of the geoscientific literature introducing tools that welcomed decision trees (Khosravi et al., 2018) and their derivatives (Abedi et al., 2021; Ghosh and Maiti, 2021), support vector machines (Liong and Sivapragasam, 2002), neural networks (Fang et al., 2021) and their most recent deep learning extensions (Chen et al., 2021). All these tools have been created to seek the best modeling susceptibility performance in a data-driven context. However, results are achieved at the expense of interpretability, something the multivariate statistical framework ensures throughout its process. For this reason, albeit in lesser numbers, the geoscientific community has branched out to welcome Generalized Additive Models (Brenning, 2008; Steger et al., 2021a), a model archetype capable of producing high performance while keeping the interpretation clear (Goetz et al., 2011, 2015).

This is the general situation regarding the modeling aspects when it comes to natural hazards. As for the regions where such hazards were studied, most of the geoscientific literature gravitated around surface processes typical of mid-latitudes. Conversely, natural hazards typical of arctic environments have received much less attention. This is mostly due to the fact that periglacial regions host a drastically smaller human population and therefore, the need for understanding and modeling cryospheric hazards has historically been less prominent than elsewhere. However, global warming is rapidly changing this situation. In fact, periglacial areas are undergoing temperature changes at a much faster rate than what happens at mid-latitudes (Rantanen et al., 2022). In turn, this implies that cryospheric hazards have become more spatially and temporally common (Ding et al., 2021), leading to very negative effects. These aspects involve for instance the destabilization of human infrastructures (Nicu et al., 2020), the modification of sediment budgets along the river networks (Crosby, 2009), and the release of greenhouse gases (Abbott and Jones, 2015). The first issue relates to the potential damage and loss of human structures, both for their current (Hjort et al., 2022) and heritage (Nicu et al., 2021) values. As for the second, river banks usually held together by ice can fail once the ice thaws, thus introducing additional sediments along the channels, which are transported and deposited far away from their otherwise stable source (Tananaev and Lotsari, 2022). Greenhouse gases also constitute a byproduct of the periglacial changes we are experiencing in recent years. The mechanism involves freeing carbon dioxide (Turetsky et al., 2020) and/or methane (Klapstein et al., 2014) into the atmosphere. These fluids were originally sealed within frozen porous materials, which once thawed, have the potential of releasing large volumes of gases (Knoblauch et al., 2013). All these phenomena share a common root cause, this being usually referred to as permafrost degradation (Streletskiy et al., 2015). Permafrost is commonly defined as soil or unconsolidated material, whose water hosted in its pores has been frozen for more than two years (Dobinski, 2011). This degradation and consequent thawing of the ice geomorphologically leads to specific landforms whose evolution is considered a natural hazard in itself. Specifically, permafrost degradation commonly gives rise to retrogressive thaw slumps (RTSs), active layer detachments (ALDs) and thermo-gully erosional features. RTS are slope failures characterized by rounded or even horse-shoe shapes, whose evolution moves backwards (therefore the term retrogressive; Lacelle et al., 2010) over several seasons. ALDs are processes of similar origin whose failure occurs much more impulsively, leading to mass movements that can transport unconsolidated materials hundreds of meters away (Kokelj and Jorgenson, 2013). As for thermo-gullies, these are also cryospheric hazards but their evolution is strongly linear and usually occurs along terrain incisions (Kokelj et al., 2017).

We mentioned before that cryospheric hazards have historically received much lesser attention compared to their mid-latitude counterparts. This is clearly reflected in the amount of data available to the geoscientific community. In turn, this limits the ability to build data-driven models aimed at predicting where cryospheric hazards may develop in the future. Currently, very few experiments exist, these being mostly carried out in Alaska (e.g., Blais-Stevens et al., 2015; Behnia and Blais-Stevens, 2018).

Aside from the data availability issues and the limited presence of human settlements, being capable of estimating whether RTSs and ALDs can develop in arctic environments could be crucial for several reasons. The most important of these is developing an understanding of cryospheric dynamics. In fact, by using uncharted arctic territory to build up experience in data-driven models for such processes, one could transfer their prediction to other areas where RTSs and ALDs may not currently exist, but their genesis will take place and increase in the years to come. For instance, the Alpine (Sattler et al., 2011) and Himalayan (Huang et al., 2020) ranges are already experiencing similar hazard occurrences. The experience gained from the arctic context, where significant temperature changes are constantly observed, could be of particular relevance to developing mitigation strategies across these mountainous regions. Moreover, within the same arctic context, understanding susceptible areas to RTS and ALDs can help quantify potential changes in sediment budgets as well as greenhouse gas releases.

With these overall aims in mind, here we tested our ability to classify the northern Alaskan landscape into locations prone to experience RTS and ALD. Also, following the idea of developing an understanding of the dynamics in periglacial areas, we selected a GAM framework, to ensure a suitable prediction together with a reliable interpretation. To do so, we exploited the large breadth of environmental information available in Google Earth Engine. Specifically, our modeling protocol that can access this cloud repository, organize, pre-process and download the necessary information to locally build GAM-based predictive models for RTS and ALD.

2 Study area and cryospheric hazard inventories

The study area is located in the Far North or Arctic Alaska, which is the northernmost region of the United States, located above the Yukon river. According to the Köppen-Geiger climate classification, the area we chose belongs to subarctic and tundra environments (Peel et al., 2007). The reason behind the choice of our study region is primarily due to data availability. In fact, Swanson (2021) recently published an article where they share a detailed inventory of RTS and ALD for the northern Alaskan landscape. In their work, the authors also well describe the state of the region in the last few decades, offering an overview of local climatic conditions and their recent evolution. Specifically, in the last forty years, the area exhibited a mean yearly air temperature between $-5\,^{\circ}$C and $-8\,^{\circ}$C. Conversely, the mean annual ground temperature from 2000 to 2009, generally ranged between $-3\,^{\circ}$C and $-8\,^{\circ}$C with local exceptions above $-3\,^{\circ}$C. However, temperatures underwent a significant increase in Alaska with time. For instance, Stafford et al. (2000) observed a $2.2\,^{\circ}$C air temperature increase during winter between 1949 and 1998. Similarly, from 1950 to 2017, Wendler et al. (2017) reported a mean annual air temperature increase of $2.1\,^{\circ}$C. These patterns are also reflected in the soil column, with an increase ranging between 1-2 °C in the Brook range, (see Osterkamp, 2005), and in the range of 0.5-1.5 °C slight eastward of our study area (Osterkamp and Romanovsky, 1999). For this reason, this Alaskan sector has been observed (Jorgenson et al., 2001, 2006) and modeled (Ling and Zhang, 2003; Jafarov et al., 2012) to be particularly prone to permafrost degradation. In turn, permafrost degradation is responsible for the thousands of cryospheric hazard occurrences mapped by Swanson (2021). Specifically, the inventory accounts for 1295 RTSs and 5508 ALDs just within ~ 50000 km^2 (Fig.1).

Notably, with the aim to test a susceptibility model both for RTS and ALD, we also selected an additional area to be used for model transferability purposes (see, Rudy et al., 2016; Cama et al., 2017). This area is shown in Fig.1, panels b and c.

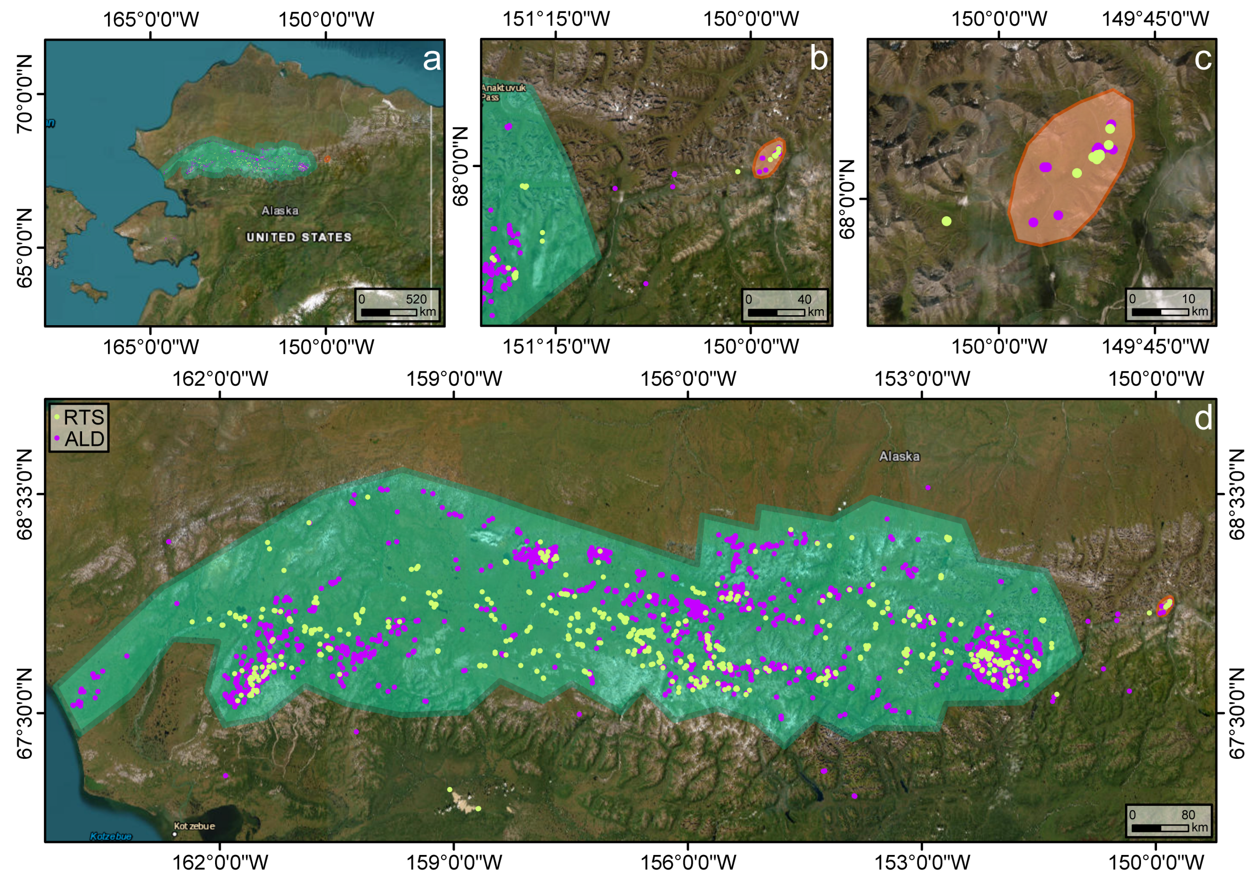

Figure 1: Panel **d** shows the study area, whose general location as part of Alaska is highlighted in panel **a**, whereas panels **c** and **d** show the location of a small dataset we used as an external validation site.

3 Material and methods

3.1 Mapping units

A fundamental requirement of any susceptibility model is the choice of a suitable mapping unit. These units are the basic spatial object upon which a given study area is partitioned and also represent the object to which the probability will be ultimately assigned. The choice usually falls on either regular or irregular polygonal partitions. The former corresponds to squared grids. For instance, these are commonly employed for wildfire (see, Leuenberger et al., 2018) or gully erosion (see, Cama et al., 2020) susceptibility mapping, or in a number of lava (e.g., Crisci et al., 2004) and debris (e.g., Avolio et al., 2013) flow modeling applications. An alternative to these regular objects can be found in slope units (see, Carrara et al., 1991), catchments (e.g., Bertrand et al., 2013) or administrative units (Günther et al., 2013). Each one of these options influences the use of the susceptibility, with detailed mapping units often being useful for local master plans and coarser ones being required to support regional or national-scale territorial management practices. In our case, we could not opt for a slope unit partition for most of the RTSs and ALDs occur also in relatively gentle slopes (where the automatic slope unit generation fails). Similarly, we did not use catchments and administrative units to avoid unnecessary generalizations of the results. Therefore, we ultimately chose a squared lattice, whose size we constrained to a 225×225 m^2 for two reasons. First, the area was so large that any smaller unit would have led to a drastic increase in computational burden. Second, a 225 m side is the same resolution as the DEM accessible through Google Earth Engine (Danielson and Gesch, 2011). Therefore, by choosing a standard reference, all subsequent operations for predictors' generation also became straightforward. Notably, any mapping unit choice is arbitrary and the main requirement to be satisfied is for a mapping unit to reflect the environmental characteristics responsible for the genesis of the process under consideration. In this sense, a 225 m side grid is close enough to represent the size distribution of the RTS (mean length = 90 m, std. length = 111 m, max length = 1117 m) and ALD (mean length = 54 m, std. length = 79 m, max length = 957 m) polygons mapped by (Swanson, 2021).

3.2 Predictors

Another fundamental requirement for any susceptibility model is the selection of a predictor set capable of explaining the distribution of presence/absence data, while respecting the physical understanding of the process at hand. In the case of cryospheric hazards induced by permafrost degradation, the predictor set has to include terrain, geological and climate-related characteristics. Here we chose a total of 11 covariates, these being listed in Table 1. Among them, the slope steepness is meant to convey the direction along which gravitational pull would act (Ramage et al., 2017). As for the slope exposition, we chose this property both as a proxy for strata attitude as well as for carrying the sunlight exposition signal in the northern hemisphere (Lacelle et al., 2015). The two curvatures are often used to indicate landscape concavity or convexity, shapes that control the acceleration of overland water flows along preferential directions (Ohlmacher, 2007). Geology is instead a proxy for the above soil column type, where RTSs and ALDs may develop (Blais-Stevens et al., 2015). As for NDVI, this is commonly used to map cryospheric hazards and also conveys the presence of vegetation disturbance (Huang et al., 2020). Ultimately, precipitation (Balser et al., 2014), thawing degree days (Lantz and Kokelj, 2008), July temperature (Jones et al., 2019), snow albedo (Cassidy et al., 2017), and snow cover (Kokelj et al., 2009) holistically describe climatic characteristics that can lead to RTS and ALS formation and their development.

We would like to stress that computing such a covariate set has historically been quite challenging. However, cloud computing solutions, such as Google Earth Engine, have made accessing, processing and downloading large data volumes a relatively easy task. To accomplish this task, we have created a Python script that essentially returns the data matrix necessary for the subsequent RTS and ALD modeling. The code is accessible at CryoS, and we made it open for anyone who would like to replicate the same analyses or run them in other areas. Notably, statistical models require removing any redundant covariate to avoid

Variable name	Shortcut	Unit	Reference
Geology	GEO	1	Wilson and Labay (2016)
Slope	SLP	degrees	Zevenbergen and Thorne (1987)
Horizontal curvature	HC	m^{-1}	Heerdegen and Beran (1982)
Vertical curvature	VC	m^{-1}	Heerdegen and Beran (1982)
Aspect	ASP	degrees	Zevenbergen and Thorne (1987)
NDVI	NDVI	1	Rouse et al. (1974)
Precipitation	PRCP	mm	Thornton et al. (2014)
Thawing degree days	TDD	# days	Boyd (1976)
July temperature	JT	°C	Wan (2015)
Snow albedo	ALB	1	Hall et al. (2016)
Snow cover	SNOWC	1	Hall et al. (2016)

Table 1: list of the predictor set we used to explain the RTS and ALD distribution of presence/absence data.

multicollinearity issues (Alin, 2010). Here, we show some preliminary analyses where we tested the pairwise correlation among the ten covariates we chose (excluding the geology; Figure 2).

3.3 GAM

We utilized a Generalized Additive Model (GAM) framework to map the Northern Alaskan landscape susceptibility to RTS or ALD, with two separate models built for each one of these cryospheric hazards. GAMs are a type of semi-parametric models that combines the flexibility of nonparametric ones together with the interpretability typical of simpler linear models (Wood, 2006). The semi-parametric nature of GAMs comes from the fact that they use a linear model as the foundation and then apply smoothing functions (i.e. non-parametric relationships, such as splines) to the predictor variables (Hastie, 2017). These smoothing functions allow the model to capture non-linear relationships between the predictor variables (covariates) and the response variable (RTS or ALD occurrence) without making strong assumptions about the functional form of these relationships (Wood, 2017). GAMs have been used in a variety of susceptibility studies, ranging from regional to local scales (Yalcin et al., 2011; Petschko et al., 2012; Titti et al., 2021).

More generally, a GAM can be used to explain data distributed according to several exponential family distributions (gamma, Gaussian, etc.; Wood, 2006). In our context, the response variable is represented by a binary dataset with zeros and ones, indicating the absence or presence of cryospheric hazards at specific locations. For this reason, the ideal framework to model presences/absences of RTSs or ALDs corresponds to the binomial case, which assumes the two separate RTS and ALD dichotomous data to behave according to a Bernoulli probability distribution (Bryce et al., 2022). A binomial GAM can be denoted as

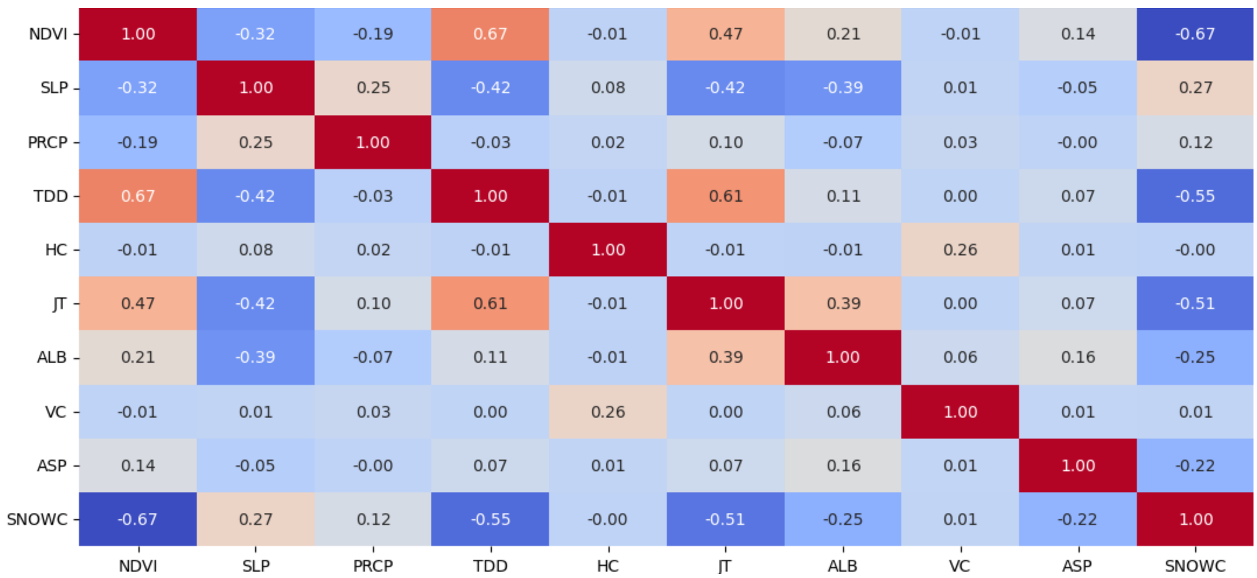

Figure 2: Pairwise correlation matrix computed between covariates. Notably, the lithology is not included because of its categorical nature.

follows:

$$\eta(\pi) = \log\left(\frac{\pi}{1-\pi}\right) = \beta_0 + \sum_{i=0}^{\#\text{ cov.}} f_i x_i \ , \tag{1}$$

where η is the logit function, π is the probability that cryospheric hazards are present at a given location, β_0 is the global intercept and f_i is the nonlinear function estimated for each of the covariate x_i in the model.

The output of a binomial GAM (Eq. (1)) is expressed as a continuous spectrum of values that reflect the probability of RTS or ALD occurrence. To evaluate the performance of binary classifiers, various metrics can be considered and grouped into two main categories: cut-off dependent (Rahmati et al., 2019) and independent (Mende and Koschke, 2010) metrics. Cut-off dependent metrics involve the selection of a specific threshold value to reclassify the probability spectrum into a binary dataset, which can be matched against the initial observations. This leads to the computation of confusion matrices, from which accuracy, precision, recall, and F1 score can be derived (Bertolini, 2021). In the remainder of this manuscript, we will use the Youden Index (for a detailed description, see Fluss et al., 2005) to estimate the best probability cutoff. In contrast, cut-off independent metrics rely on multiple probability thresholds to compute true positives and negatives, as well as false positives and negatives. These metrics include the receiver operating characteristic (ROC; Hosmer and Lemeshow, 2000) or the precision-recall curves (PR; Loche et al., 2022) and their respective area under the curve (AUC; Boyd et al., 2013; Hajian-Tilaki, 2013).

Binary classifications can be used both for explanatory (Lombardo and Mai, 2018) and predictive purposes (Lima et al., 2021). Explanatory assessments involve interpreting the functional relations estimated from multi-variate regressions of the presence/absence vector with respect to the covariate set; i.e. the model seeks to explain why and where these hazards take place, by identifying key factors and variables that influence their occurrence and distribution (Steger et al., 2021b). This can be done using the full available information, as in our work, fitting 100% of the grid cells in our study area. However, the estimated results cannot be directly interpreted for predictive purposes. Prediction is here intended as a probabilistic estimation over unknown areas (spatially) to a given classifier that has been trained elsewhere. The aim, in this case, is to estimate areas where the processes may currently be absent, but their terrain and environmental characteristics imply that they could manifest in the future (temporally). To pursue this goal, two common approaches are used instead. The most natural approach consists of measuring the prediction skill with subsequent hazard occurrences (Lombardo and Tanyas, 2020). However, this is rarely done due to the scarcity of multi-temporal hazard inventories Guzzetti et al. (2012). Therefore, when only spatial data is available, a common routine for estimating predictive performance involves splitting the data into a portion used for calibration and another for validation. This assumes that spatial replicates mimic the behaviour of temporal ones. Also, the training and test splits can be done in different ways. The simplest approach is pure random split, leading to the so-called random cross-validation (RCV; Roberts et al., 2017). However, this usually leaves the data structure unchanged, resulting in similar performances to the calibration ones. Another approach is commonly referred to as spatial cross-validation (SCV; Brenning, 2012), which uses a spatially constrained subset of the data and allows for the assessment of how well the model performs in specific sectors of the study area. SCV can reveal localized model performance, which RCV cannot detect.

This study makes use of all elements described above. The two cryospheric hazard data sets are used to generate separate presence/absence instances, whose entire information is fitted to the covariate sets computed for the Far North Alaska landscape. As a result, the model output is suitable for interpretation, allowing for the exploration of each covariate effect. As for assessing the models' predictive skills, we perform two cross-validations (a 10-fold RCV and an 10-fold SCV), for both RTSs and ALDs. Finally, we tested the fitted model on a small test area eastward of the study area, as an additional mean to evaluate the model generalization (Figure 1).

We stress here that, the binomial GAM protocol we developed as part of this research is implemented in Python (Servén and Brummitt, 2018), using the pyGAM package (Servén and Brummitt, 2018). With it, we developed a fully functional routine that, through Python, accesses cloud-based data on Google Earth Engine, processes it and then elaborates it, all with the same script available on GitHub (CryoS).

3.4 Stepwise GAM

In the literature, several solutions are available to perform variable selection, including stepwise procedures (Atkinson and Massari, 1998; Beguería, 2006; Meusburger and Alewell, 2009), LASSO (Castro Camilo et al., 2017; Amato et al., 2019; Deng et al., 2021) or penalization and more. Here we implemented a stepwise forward selection routine as part of the best GAM model selection. Stepwise forward selection (SFS) is an iterative approach that aims at identifying the optimal set of variables that strikes a balance between performance and simplicity, reducing overfitting and improving the generalizability of the model Khan et al. (2007). This method boils down to building one model at a time, starting from the best single variable, then moving to the best couple, triple and so on, sorted according to the Akaike Information Criterion (AIC; Hu, 2007). The algorithm continues to add variables one by one until there is no significant improvement is achieved by adding further covariate information. At this point, the algorithm stops and returns the final set of predictor variables that provide the best predictive power while keeping the model simple and parsimonious.

In other programming environments such as R, stepwise GAM functions are available (see step.GAM in Hastie and Hastie, 2015). However, in Python this is not the case. For this reason, we implemented our own local "step.GAM" routine in Python and also share it as part of the code accessible at (CryoS).

4 Results

In the following paragraphs, we show the results of the binomial GAMs both for RTSs and ALDs susceptibility and both for the study and test areas.

4.1 Variable selection

Figures 3 show the results of the SFS for both RTS and ALD binomial GAM models. In the ALD model, all variables were retained (Figure 3b), whereas in the RTS model, the last three variables (namely, SNOWC, ASP and TDD) were excluded as they did not contribute to the model's performance, i.e. the AIC does not exhibit any significant decrease. Interestingly, while storing AIC values at each stepwise iteration, we also stored the AUC goodness-of-fit values, which are also reported in Figure 3b. In both RTS and ALD cases, the AIC and AUC curves show almost perfectly inverted patterns. For instance, in the case of RTS, even the AUC curve reaches an asymptote at JT, justifying the exclusion of SNOWC, ASP and TDD. Similarly, in the case of ALD, the AUC continuously increases up to the last covariate insertion.

4.2 Susceptibility modeling performance

We measured both the goodness-of-fit and predictive skills. To do so, we used ROC and AUC values, both for the reference fitting procedure and two types of cross-validation, namely a 10-fold Random Cross-Validation (RCV) and a 10-fold Spatial Cross-Validation (SCV). Regarding the latter procedure, the spatial subdivision utilized for both models was generated by performing a k-means clustering of the coordinates of the study area's pixels. Figure 4

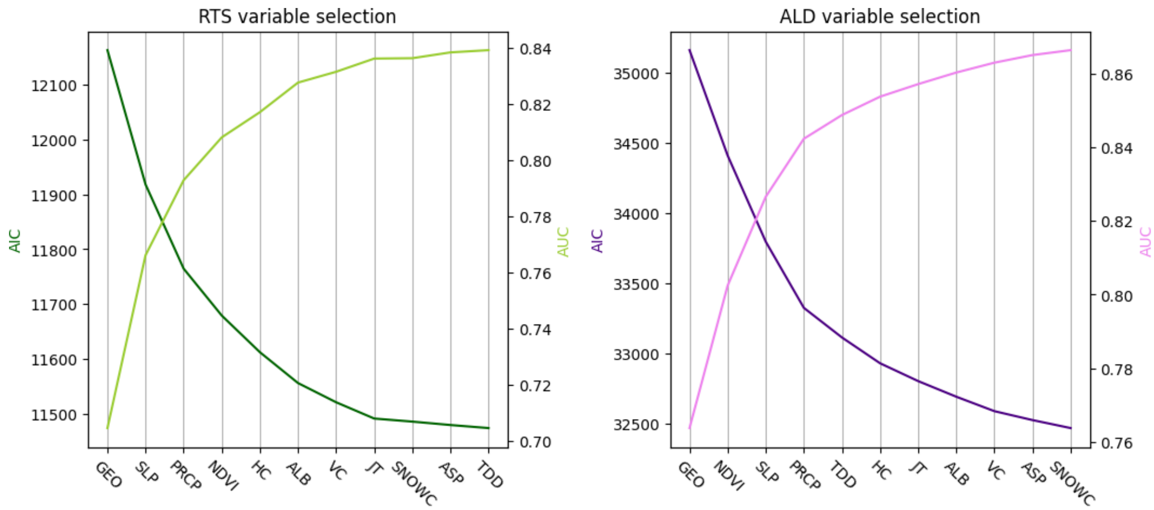

(a) Variable selection for RTS binomial GAM model.

(b) Variable selection for ALD binomial GAM model.

Figure 3: Variable selection for RTS and ALD binomial GAM models. The dark and light curves show the behavior of the AIC and the AUC in the SFS, respectively.

provides a visualization of the resulting subdivision where each area marks the leave-one-out procedure used for validation.

The results (Figure 5) show that the performance of the model falls within the "excellent" category according to the AUC classification proposed by (Hosmer and Lemeshow, 2000). However, upon closer inspection, the fit and RCV results are better, falling almost within the "outstanding" category (with means above 0.8 and below 0.9). The lower performance exhibited for SCV was not surprising, and in fact, it serves as an important indicator of the prediction skill of our model under a blind test, where the model cannot rely on its native spatial structure.

In other words, a spatial cross-validation usually returns the worst-case scenario performance in any spatial model. This is also particularly evident when examining the uncertainty across bootstrap replicates and cross-validation type. In fact, the variability for RCV is particularly low since the random selection does not disentangle local spatial dependence in the data. As for SCV, where the spatial dependence was perturbed due to the constrained local selection, the variability is much higher, although still within an acceptable range (acceptable AUC threshold = 0.7; Hosmer and Lemeshow, 2000). Specifically, for the ALD case, 10 out 10 replicates exceed the 0.7 AUC mark. Conversely, for the RTS case, 7 out 10 replicates do the same.

Another way to elaborate on model performance is to look at confusion plots (see, Amato et al., 2021), where the model accuracy is decoupled for presence and absence data. These are shown in Figure 6, for both RTS and ALD, as well as for the results obtained from the fit, RCV and SCV. At a first glance, the figure quickly illustrates that the variation between the fitted model and the two cross-validation tests appears to be quite small for

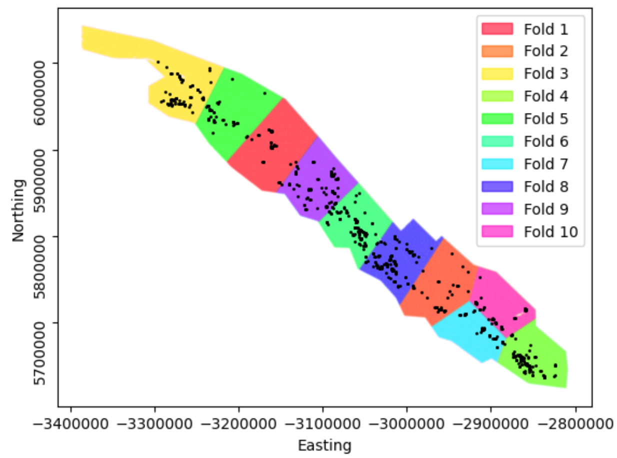

Figure 4: Geograpical illustration of the ten spatial subsets used for the tenfold SCV. The two panels show the spatial subdivisions used in the RTS and ALD models, respectively. The black dots are the locations of the two cryospheric hazard.

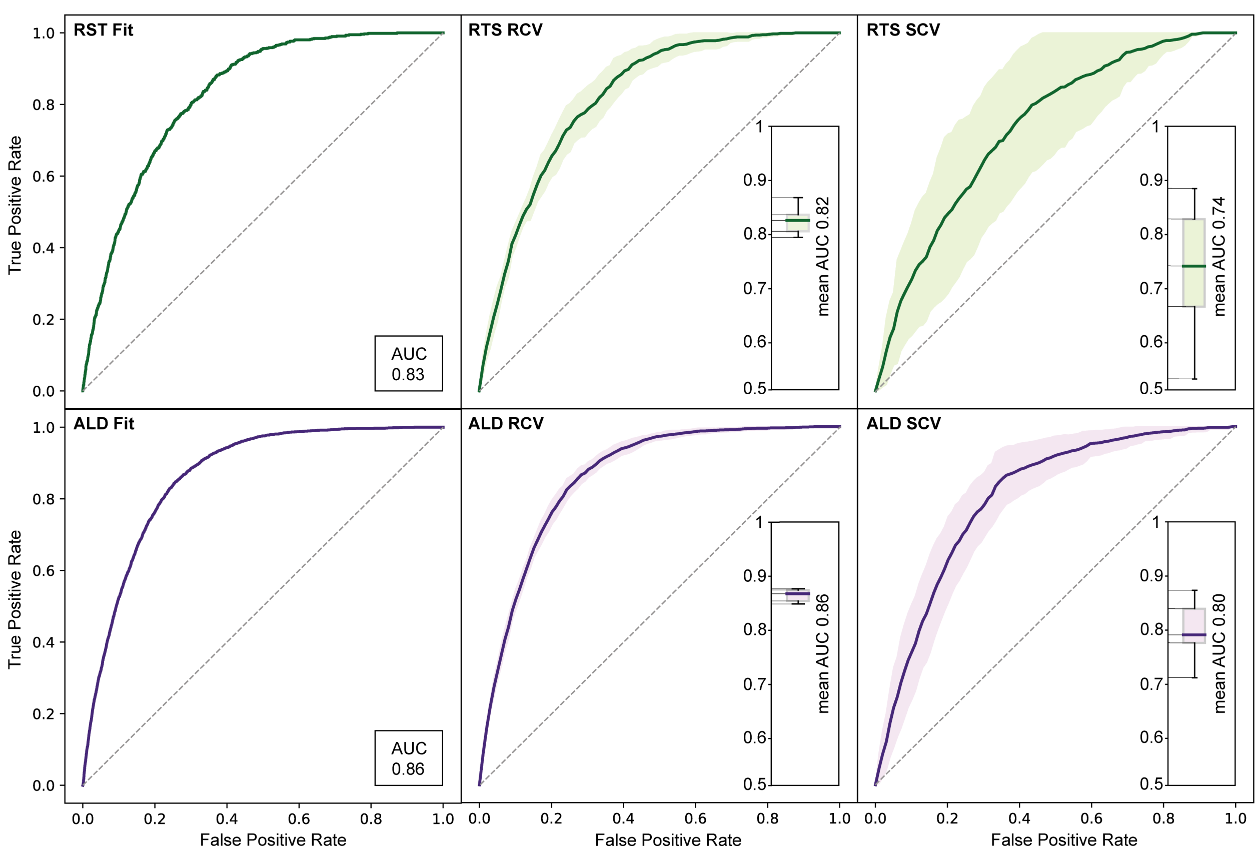

Figure 5: Modeling performance overview. First row indicates the results for RTSs, whereas the second row reports the ALDs. The thick lines for the two cross-validation schemes represent the mean ROC curve, whereas the filled area show the variability in the cross-validation scheme via a single standard deviation.

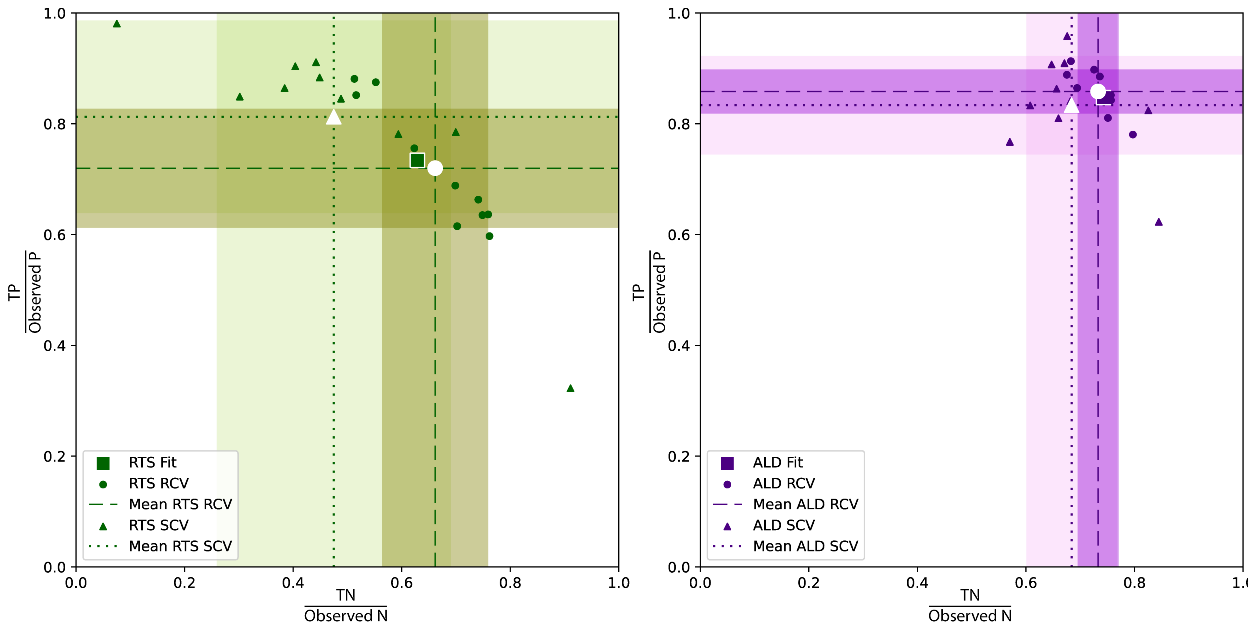

Figure 6: Confusion plots for RTS and ALD. The square symbols indicate the results obtained from the fit. The circles refer to the RCV whereas the triangles refer to the SCV. The colored bands indicate the variability in the ten cross-validated replicates. As for the white symbols, they represent the mean behavior obtained for the two cross-validations.

the ALD case. This can be inspected by looking at the distance between the fit results (the only square symbols), comparing their position to the white symbols, which constitute the mean behavior of the two cross-validations. The same consideration is valid when looking at the uncertainty bounds. These are measured with a single standard deviation width from the mean, showing much narrower intervals for the ALD as compared to RTS. Aside from the relative assessment, the two models still appear to the performing well also in absolute values, with even the RTS results being associated with accurate estimates, with very few exceptions.

The last attempt to showcase our model is shown in Figure 7. There, the susceptibility patterns are obtained by locally solving the prediction function fitted over another study area. This procedure is commonly referred to as model transferability (Steger et al., 2022) or as validation with independent spatial data (Roberts et al., 2017) and it is often assumed to return worse performance as compared to tests that are run within the same study area where a given model is calibrated. This is confirmed even in this case, with barely acceptable transferred performances down to 0.7 of AUC in both cases.

4.3 Covariates' effects

To evaluate the covariates' effects on the final susceptibility estimates, we generated partial dependence plots for each covariate. These plots provide a visual representation of the relationship between the predictor variables and the response variable, allowing us to assess

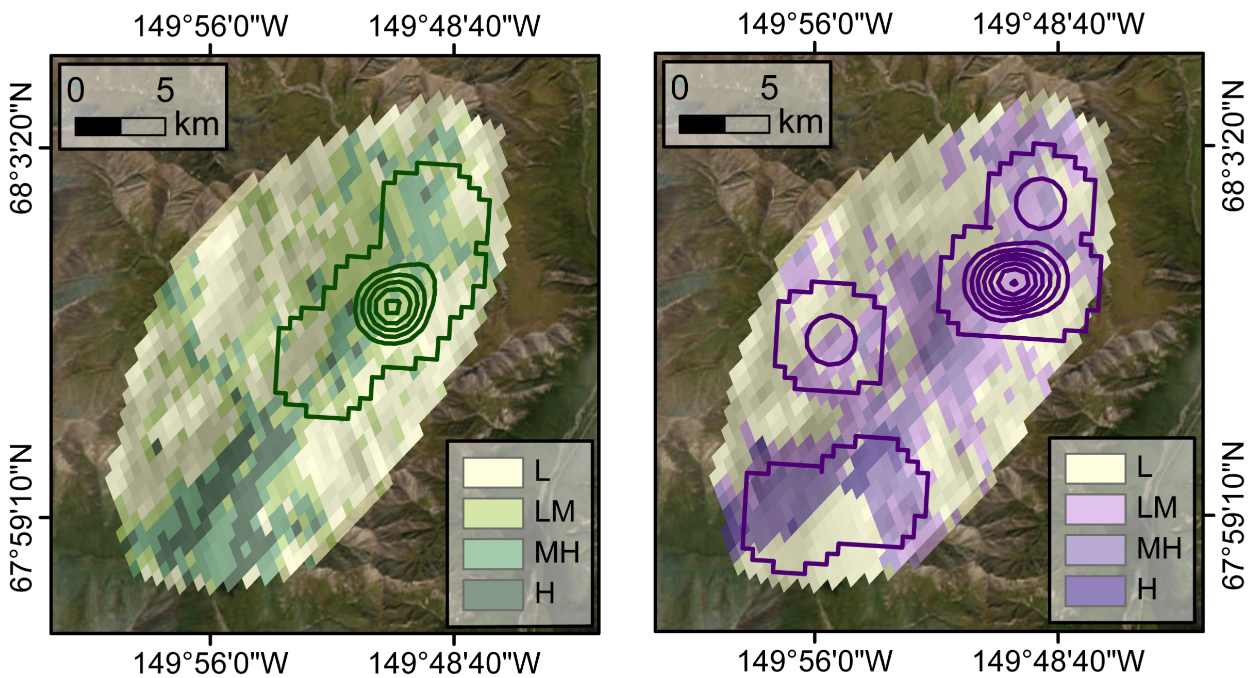

Figure 7: Model transferability tests: the left panel shows the RTS susceptibility (AUC = 0.7). The right one shows the ALD case (AUC = 0.7). The contour lines correspond to the density of cryospheric hazards per km^2.

the impact of each covariate on RTSs and ALDs susceptibility, separately. The partial dependence plots for each term of the model are shown in Figure 8 and 9. Notably, to improve readability, we have opted to plot the y-axis directly in the response scale (as probabilities) rather than in the linear predictor scale (as regression coefficients).

The two figures reveal that there are some notable similarities in the way certain covariates are influencing RTSs and ALDs occurrences. However, there are also marked differences between the two, suggesting that the covariates may be playing distinct roles in each process. Below we will present our interpretation for each covariate and for each of the two processes under consideration.

Geology (GEO) The association of RTSs and ALDs with bedrock lithology can be difficult to analyze in permafrost regions due to several factors. In particular, these processes typically occur on the surface sediment of the active layer, rather than directly at the bedrock level. Our RTS (Figures 8 and ALD 9) models showed that the lithologies belonging to the Endicott group (denoted with the numbers 6, 10, 13, 23; Appendix A) underlay areas prone to RTSs and ALDs occurrence (i.e., contributing with marginal probabilities consistently above 0.8 for each lithotype). The Endicott group is a type of clastic sequence consisting mainly of shale, sandstone, and conglomerate (Tailleur et al., 1967). From an interpretative standpoint, the constant positive contribution of such materials may reflect the potential instability of unconsolidated materials, as opposed to more massive and cohesive ones dis-

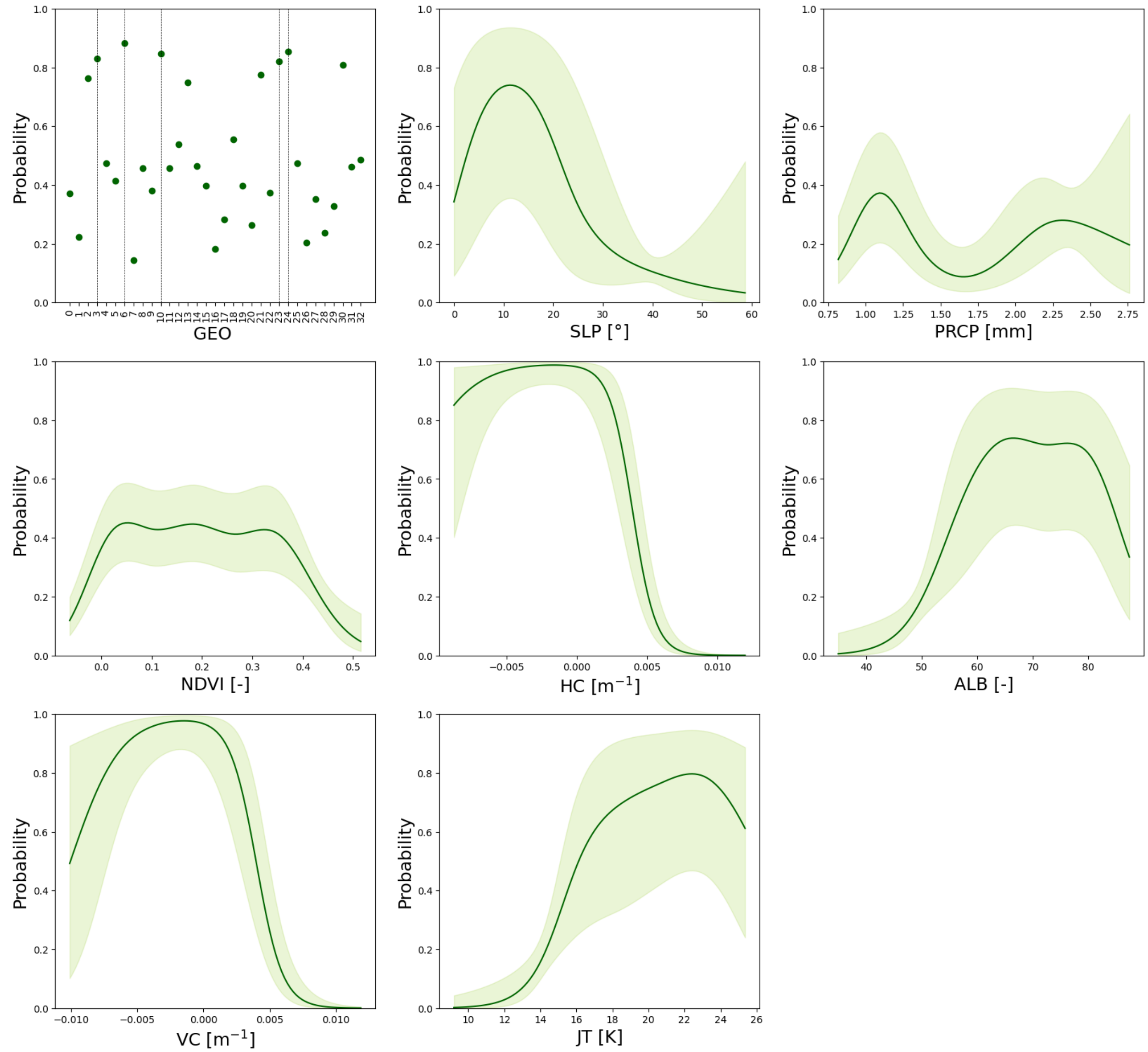

Figure 8: Marginal plots of the covariates' effects estimated for the RTS susceptibility model. Notably, the y-axes are directly expressed at the response scale (in probability rather than at the scale of the regression coefficients).

tributed over the study area. Likely, when the permafrost is healthy or in normal conditions, these materials are held together by the ice structure. However, when the permafrost starts to degrade, this clastic sequence is the first one in the area that experiences instability, something that both models statistically picked up, irrespective of the cryospheric hazard under consideration, The last lithotype worth to be mentioned corresponds to North Alaska Sedimentary rocks (denoted with number 24 in the figures and in Appendix A). Interestingly, this appears to promote RTSs (marginal probability = 0.85) and oppose ALDs (marginal probability = 0.26). One of the possible interpretations is that these sedimentary rocks are reported by Dillon et al. (1986) to have been mapped as part of the same formation, although

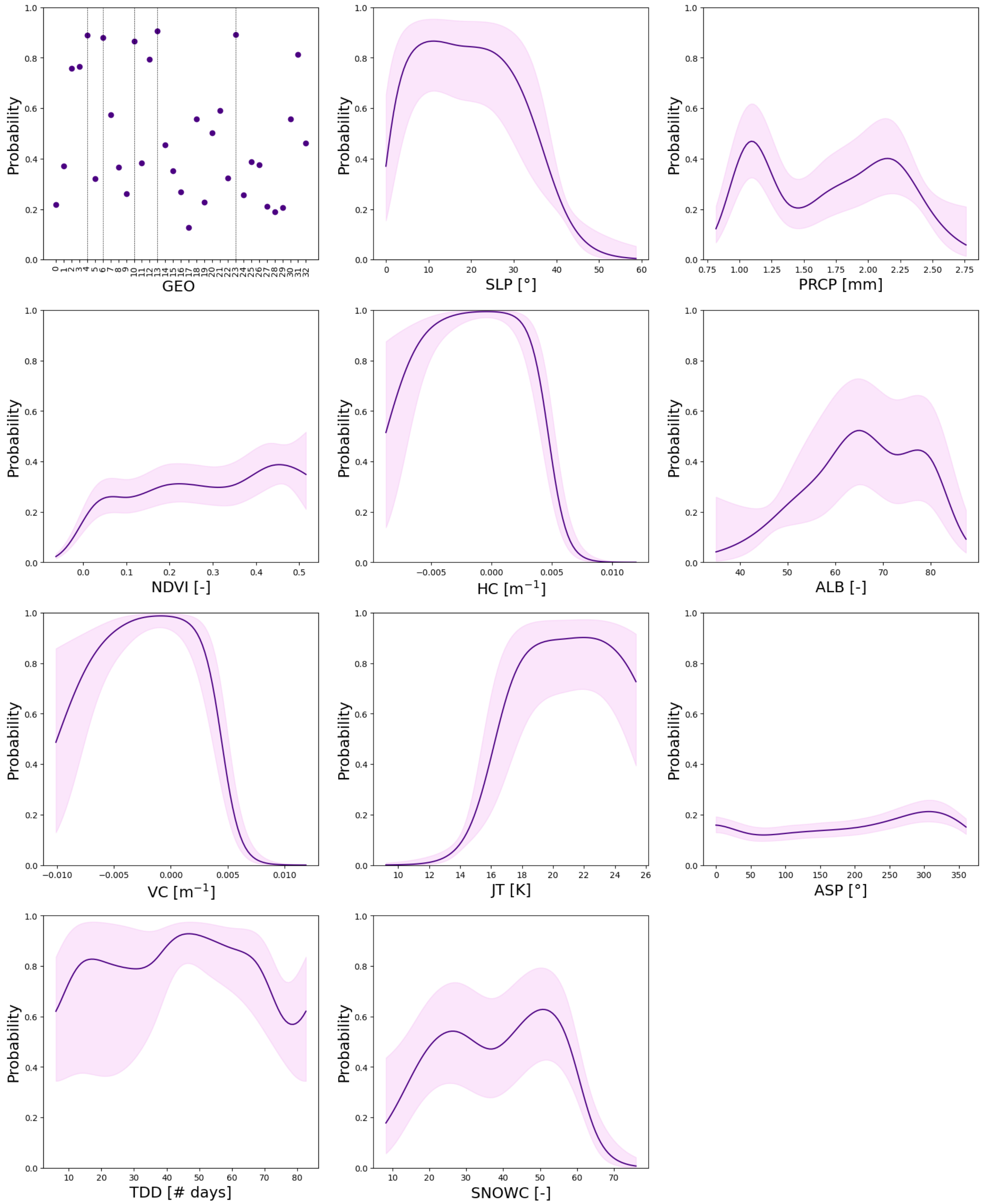

Figure 9: Marginal plots of the covariates' effects estimated for the ALD susceptibility model. Notably, the y-axes are directly expressed at the response scale (in probability rather than at the scale of the regression coefficients).

they internally exhibit a significant degree of anisotropy due to the different nature of the constitutive material and relative granulometry. It is possible that the same anisotropy may favour one cryospheric hazard rather than the other, as a function of the respective failure mechanisms.

Slope (SLP) These partial dependence plots (Figure 8 for RTS and 9 for ALD) show that two cryospheric hazards generally behave with a similar probability decay at increasing slope gradient. However, some differences arise when looking at the covariate contribution in the first part of the slope range. Specifically, the probabilistic occurrence of the two processes increases with SLP up to 10°. RTSs become much more unlikely after this threshold, while ALDs continue to show high occurrence probabilities (> 0.8) up to 30°. This indicates that RTSs may tend to form in relatively flat areas.

At the same time, ALDs can occur along steeper morphologies, presumably because of the higher shear stress provided by this terrain morphology (Balser et al., 2014).

Horizontal curvature (HC) and Vertical curvature (VC) Areas with concave HC (i.e., negative values) are both prone to develop RTSs and ALDs (Figures 8 and 9, respectively). These morphologies indicate terrain where water fluxes converge. This may lead to erosion along the central track (Ohlmacher, 2007), a phenomenon that can start the development of cryospheric hazards. As for the transition from linear to convex landscape curvatures, the probabilities drastically drop to zero.

The partial dependence plots of VC are similar to the HC ones. Negative values of VC correspond to convex morphologies along the topographic profile. Profile convexity is responsible for vertical overland flow accelerations and therefore, similarly to the previous interpretation, the associated erosion (Ohlmacher, 2007) could lead to the formation and development of the two processes under consideration. The transition to positive VC values here indicates upwardly concave shapes, where the probability of both RTSs and ALDs become much lower.

Snow Albedo (ALB) Snow albedo (ALB) is an important parameter for determining the energy budget in high-latitude regions in winter (Li et al., 2023). The albedo effect generated by snow is generally much higher than that of other land cover types (Chapin III, 1993), and it is significantly associated with the solar radiation between the snow and atmosphere (Randall et al., 1994). ALB depends on many factors, including snow depth, snow age, vegetation coverage, vegetation canopy height, snow grain size, and internal mixing, but generally, its value varies between ∼0.6 and ∼0.9. This range corresponds to old and new snow, respectively. Values lower than 0.6 are typical of a less dense snow cover. Partial dependence plots (Figures 8 and 9) showed that ALB has a similar impact on RTSs and ALDs susceptibility models. In both cases, the maximum marginal probabilities are reached between 0.6 and 0.8 mean annual ALB, suggesting that areas covered by snow for most of the year are more likely to produce RTSs and ALDs. This is potentially the case because of the specific information carries in the range $0.6 < \text{ALB} < 0.8$. Values below 0.6 may indicate locations where little to no snow is available through the year and, therefore, where permafrost is not available to behind with. As for values above 0.8, we enter the domain of a very dense snow mantle, which may persist for most of the year. Conversely, the in-between range may favor cryospheric hazards because. For instance, snow-packs melting can increase the amount of free water. This gives rise to pore water pressure increase which is translated into a reduction of effective stresses at the thaw front (Lewkowicz, 2007). This mechanism is documented in several articles (e.g., Lewkowicz, 2007), together with the resulting presence of sliding events, whose manifestation is due to the combined action of the snow cover melt and the rapid thaw of the ice-rich transient layer (e.g., Lamoureux and Lafrenière, 2009).

In any case, a general interpretation is that the albedo reduction occurring after snow melt leads to a positive change in the energy budget at the Earth's surface. This may contribute to the deepening of the active layer (Streletskiy et al., 2015; Zheng et al., 2019), thus promoting the formation of RTSs and ALDs.

July temperature (JT) Summer temperatures directly play a critical role in the formation of RTSs and ALDs, as higher temperatures can lead to more extensive permafrost thaw and ground surface instability. Several studies have shown a positive correlation between summer temperatures and the occurrence of RTSs and ALDs (e.g., Shiklomanov et al., 2010; Liljedahl et al., 2016). Looking at both the marginal plots, the JT contribution to RTSs and ALDs occurrences also reflects the same physical assumption mentioned above. In fact, high marginal probabilities are reached between 18° and 22° (see Figures 8 and 9). Beyond this temperature range, a slight decrease can be noted in the probability of RTSs and ALDs, which may suggest that these regions, characterized by higher mean JT values, are less likely to be covered by permafrost or may have more sporadic permafrost coverage.

Thawing degree days (TDD) This work defines thawing degree-days (TDD) as the number of days in a year in which surface air temperature is above zero. Therefore, TDD are used as a proxy measure of the amount of heat accumulated over a certain period and above a specific temperature threshold. This threshold is set at the level required to thaw frozen ground or ice. As a result, TDD are used to estimate the timing and duration of the spring thaw, which can affect soil moisture and water availability, hence the impact of climate change on permafrost and cryospheric hazards.

The partial dependence plots show a correlation between TDD and ALDs occurrence, highest and most meaningful for TDD between 40 and 60 days in a year (see Figure 9). Above the 70 days' mark, the marginal probabilities are characterized by a slight drop, which may be related to the absence or poor permafrost coverage in regions that experience warmer temperatures during the year.

Snow cover (SNOWC) Snow cover (SNOWC) impact on ALDs can be interpreted in a similar way as TDD and ALB. Regions characterized by low (< 20) or high (> 60) SNOWC are less prone to generate ALDs: on the one hand, permafrost is either absent or has a limited extent; hence there is not sufficient material to generate ALDs. Conversely, a high snow cover could prevent thawing and freezing cycles, thus avoiding the generation of ALDs.

4.4 Susceptibility mapping

This section translates the model results into map form. These are shown in Figure 10, where the first element to be addressed is the different probability range reached by the models, for RTS and ALD respectively. In the first case the probability reaches a maximum of 0.02, whereas, in the second, the maximum is 0.07. We recall here that we used all the information in the study area. Therefore, we have kept the natural proportion of cryospheric hazards' presences/absences towards unbalanced data sets. The greater number of ALD occurrences in the database has repercussions in the estimation of the global intercept, which is greater compared to the one estimated for the RTS. This in turn leads to a larger maximum between the two susceptibilities. Aside from these technical aspects, one of the most important considerations that arise from the two maps' observation is the way the two probability patterns appear. In fact, despite the two cryospheric hazards sharing the same genetic process in the form of permafrost degradation, they do not occupy the same landscape niches. In other words, the two susceptibility maps are significantly different and further consideration of these aspects will be provided in the multi-hazard overview. For now, another model characteristic to be highlighted links back to performance considerations. The two separate models seem again to work extremely well, with the confusion matrix showing very high counts of true positives with respect to the total, both for RTS ($\mathrm{TP}_{\mathrm{RTS}}/[\mathrm{TP}_{\mathrm{RTS}} + \mathrm{FN}_{\mathrm{RTS}}] = 88\%$) and ALD ($\mathrm{TP}_{\mathrm{ALD}}/[\mathrm{TP}_{\mathrm{ALD}} + \mathrm{FN}_{\mathrm{ALD}}] = 87\%$). This attests to the model's capacity to recognize susceptible locations. The complementary information is shown in the very low false positive counts for both. Focusing on the stable locations, these appear to be associated with high numbers of true negatives but also with high numbers of false negatives. The latter represents the most important information retrieved in this study. In fact, if we have shown that our respective models are able to accurately recognize susceptible locations to RTS and ALD, this implies that the high numbers of false positives may constitute locations where cryospheric hazards have not developed yet. In other words, the locations labelled as false positives are the ones that may generate RTS and ALD in the future.

4.5 Multi-hazard susceptibility mapping

The last part of the analyses is dedicated to the combination of the two susceptibilities into a single multi-hazard prediction map. This is a tool that offers the added value of presenting where two or more processes are more likely to occur (Lombardo et al., 2020). For this to be done though, the continuous spectra of RTS and ALD susceptibility need to be binned into

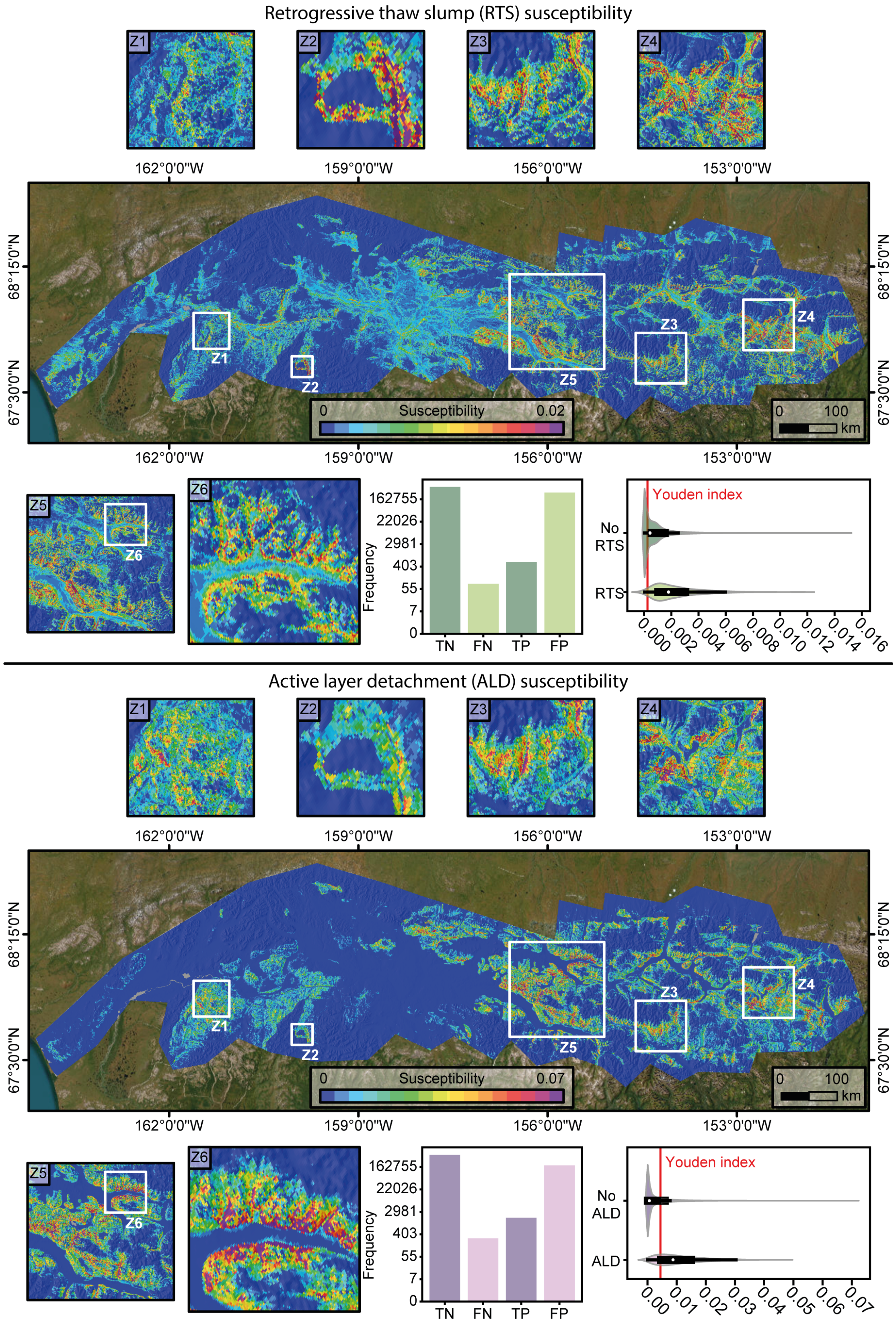

Figure 10: Susceptibility maps and associated descriptive statistics for RTS (first row) and ALD (second row). The confusion matrices shown in the barplots are obtained using the Youden Index shown in the violin plots.

a few classes. Here we chose the Fischer-Jenks method (Jenks, 1967). This procedure only requires the user to define the number of classes. Then an iterative procedure will select the thresholds that would lead to the minimum internal variance across bins (for more details, see Chen et al., 2013; Aguilera et al., 2022). We opted for four classes, whose combination returned the 16 multi-hazard levels shown in Figure 11. There, in the western sector of the study area, neither RTS nor ALD are likely to develop. However, the situation rapidly transitions to the central sector, where the landscape appears to be susceptible to both and becomes much more scattered to the east. This type of visualization maximizes the available information and can support decision-makers in prioritizing risk reduction investments (Nicu et al., 2023).

5 Discussion

This section is dedicated to discussing our modeling protocol and its results, highlighting potential strengths and weaknesses.

5.1 Supporting arguments

The number of susceptibility studies dedicated to cryospheric hazards and their impact is becoming more frequent (Nicu and Fatorić, 2023), although the situation is still far from what is typical at mid-latitudes, for other types of geomorphological processes (Reichenbach et al., 2018). Our work attempts to bridge the gap between the two worlds, testing state-of-the-art data-driven solutions in peri-arctic conditions. The Alaskan territory is one of the most studied areas in relation to RTS (e.g., Swanson and Nolan, 2018) and ALD occurrences (Blais-Stevens et al., 2014). However, a comprehensive cryospheric hazard assessment of Northern Alaska was still missing, especially considering multi-hazard aspects. This gives our experiment an additional value, although we mainly focused on methodological aspects. In fact, our work presents a protocol where the whole analysis can be essentially run in a single computing environment. Unfortunately, this is rarely the case (see, Titti et al., 2022b). In fact, even with our current technology, most of the published research in geospatial hazard modeling relies on different platforms to perform different steps of any analytical procedure.

Beyond computational considerations, our protocol offers both interpretation and high performance. This is because of our GAM choice, a particularly suitable modeling framework to explore and study covariate influences on spatial processes such as RTS and ALD. Specifically, the marginal plots offer a unique opportunity to understand how landscape and environmental characteristics may be responsible, at least probabilistically, for the two cryospheric hazard occurrences. As for the performance, both processes have been separately classified with excellent classification results across fit, RCV and SCV. The only moment where our models really suffered corresponds to the external validation performed by transferring the prediction in an area to the east. There, the results barely reached acceptable performances. However, this is mostly due to different outcropping lithologies in the area.

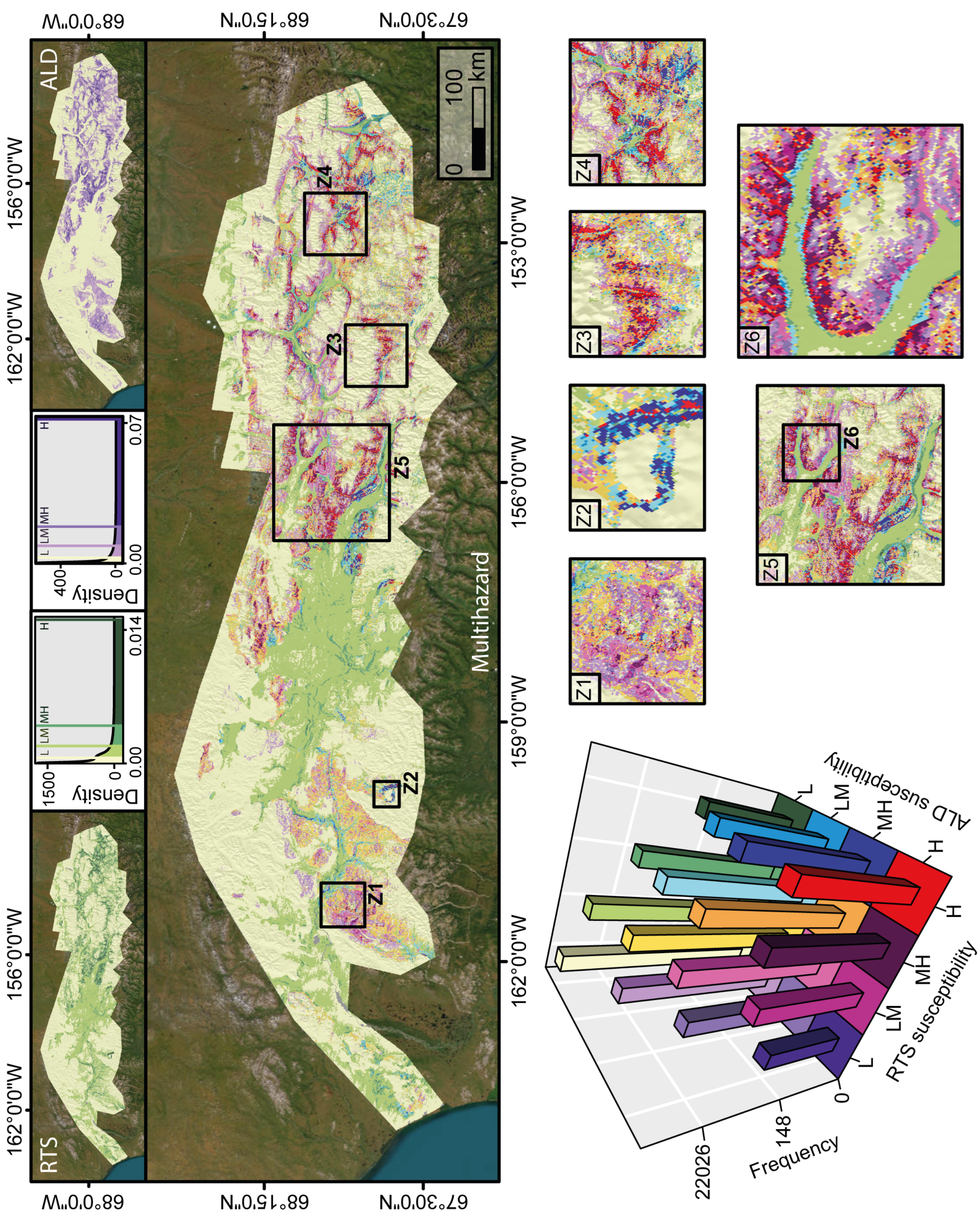

Figure 11: Multi-hazard susceptibility map. The RTS and ALD classes (four each), are defined using the Fischer-Jenks method, whose results are shown in the respective density plots. A two-dimensional barplot presents the distribution of the 16 multi-hazard classes over the study area.

This aspect of the model transferability is rarely accounted for in susceptibility studies, with only a few valid exceptions to this rule (Wang et al., 2022b). Here we highlight the model prediction skills both through external validation as well as through a spatial-cross validation routine. This is also something that methodologically is usually underreported or even entirely neglected in susceptibility modeling (Goetz et al., 2015). However, it provides a unique perspective on model performance. In fact, when the cross-validation of choice falls under the traditional random option, the model essentially stays the same, thus returning analogous performance to the fit. In other words, the perturbation the cross-validation applies to the data, compared to its original structure, is not enough to disrupt spatial autocorrelation effects from one replicate to another. This is not the case for spatial cross-validations, where entire chunks of spatial data are removed. The difference between types of cross-validations raises an important question, regarding which one of the two measures one should trust the most. In the context of geohazard modeling, one often seeks and calibrates decisions based on the worst-case scenario. For this reason, we believe the SCV to be the procedure that mimics the most how bad a model can perform and the extent to which one could rely on it. Similar considerations and concerns can already be found in Brenning (2012), although most of the research on data-driven approaches mostly disregards them.

5.2 Opposing arguments

We consider the notion of model transferability to be of particular relevance in the context of this experiment and for cryospheric hazards in general. In fact, if we have shown that the model performance substantially decrease few tens of kilometers away from the main study area, then we should ask how generalizable would our model be for instance covering the whole Alaskan territory? Our expectation is that it would likely worsen, even beyond the acceptability limit. To test this hypothesis, one would need rigorous RTS and ALD mapping standards, and public repositories to promote data-driven research. For instance, coseismic landslides (Tanyaş et al., 2019; Lombardo et al., 2021) and their rainfall-induced (Stanley and Kirschbaum, 2017; Wang et al., 2022b) counterparts have some global susceptibility solutions. However, such standards or at least such global repositories do not exist for processes generated by permafrost-degradation. To provide the right foundations to create global models or even better-constrained regional ones, data-sharing initiatives like the one promoted by Swanson (2021) should become commonplace. Unfortunately, without them, even efforts to employ state-of-the-art solutions to cryospheric hazard prediction will be very limited spatially.

Aside from the spatial aspects, another limitation of our model and in general of the majority of RTS and ALD studies is that if data is geographically scarce, when it comes to the temporal dimension it becomes almost non-existing. Extremely few exceptions do exist (see Balser et al., 2014), but they are confined to site scales. However, new developments in automated mapping may constitute the solution. Very recently, deep-learning routines have been develop to map RTS (see, Nitze et al., 2021; Yang et al., 2023), although most of the applications have been placed in Tibet (Huang et al., 2020, 2021) and only a few are available in high-arctic regions (Witharana et al., 2022). In the case of ALD, their occurrence has been mapped through change-detection (Rudy et al., 2013). Irrespective of the cryospheric hazard type, these routines are yet to be consistently used to produce multi-temporal cryospheric hazard inventories. For other hazards such as floods (James et al., 2021), landslides (Amatya et al., 2021) or fires (Anderson-Bell et al., 2021) this is already the case. The generation of RTS, ALD but also thermo-gully inventories annotated with their spatial and temporal occurrence information could unlock space-time modeling applications. In the current state, we use the term predictive model to address our GAM. However, this is only correct from a strict technical perspective. In a data-driven context, prediction is a term dedicated to a model that estimates occurrences for data that it was never trained with. However, the common definition of prediction also includes, if not even exclusively, temporal aspects such as when or how frequently a given phenomenon manifests. For this reason, we already envision possible extensions to our spatial GAM towards their space-time counterpart (e.g., Wang et al., 2022a). This could also unlock the use of the same routine for simulation purposes, moving away from the spatio-temporal domain under consideration and opening up predictions for targeted climate scenarios.

6 Conclusions

We propose a modeling protocol to estimate locations prone to develop RTS and ALD, and summarise this information in a multi-hazard susceptibility map for Northern Alaska. The binomial GAMs we test here follow the state-of-the-art in susceptibility modeling. However, we already envision future improvements that will provide the protocol presented here with a much more useful connotation for hazard and risk assessment in peri-glacial landscapes. We are currently testing deep-learning architectures to map RTS and ALD occurrences within the same study area. These architectures are being trained to recognize the same inventory mapped by (Swanson, 2021) through the optical information collected by PlanetScope (e.g., Bhuyan et al., 2023) and Rapid Eye (e.g., Kearney et al., 2020) products. Such tools can unlock multi-temporal RTS and ALD inventory mapping. From their spatiotemporal distribution, we then plan to build space time data-driven models trained with climate-related properties (e.g., rainfall and temperature), through which we could simulate probabilistic scenarios at given global warming targets. Moreover, automated mapping could also allow modeling RTS and ALD planimetric surfaces for hazard assessment purposes, extending the study area and more. Our plan is to share the results in the same way as we shared codes and data as part of this experiment, in the hope of promoting research on cryospheric hazards modeling.

A Geology

#	Geology (GEO) name
0	Akmalik Chert and other black chert of the Lisburne Group
1	Baird Group and similar rocks
2	Beaucoup Formation, undivided
3	Bedrock of unknown type or age or areas not mapped
4	Bimodal metavolcanic rocks
5	Brooks Range schist belt
6	Endicott Group, undivided
7	Etivluk Group, undivided
8	Gneiss of northern Alaska
9	Granitic rocks and orthogneiss
10	Hunt Fork Shale (Endicott Group)
11	Igneous rocks (Angayucham)
12	Kanayut Conglomerate and Noatak Sandstone, undivided (Endicott Group)
13	Kayak Shale (Endicott Group)
14	Kingak Shale, Shublik Formation, and Karen Creek Sandstone, undivided
15	Kuna Formation (Lisburne Group)
16	Lisburne Group, undivided
17	Mafic and ultramafic rocks in central, western, and northern Alaska
18	Marble
19	Metasedimentary and metavolcanic rocks of Mount Angayukaqsraq
20	Metasedimentary and metavolcanic rocks of Tukpahlearik Creek, undivided
21	Metasedimentary and metavolcanic rocks of the Central Belt and Northern Thrust assemblage of Till and others (2008a)
22	Nasorak and Utukok Formations (Lisburne Group)
23	Noatak Sandstone (Endicott Group)
24	Northern Alaska sedimentary rocks
25	Nuka Formation
26	Okpikruak and Kongakut Formations
27	Older carbonate rocks of northern Alaska
28	Older rock units of the Doonerak Window
29	Tupik and Kogruk Formations (Lisburne Group)
30	Unconsolidated and poorly consolidated surficial deposits
31	Volcanic rocks and sills
32	West-central Alaska melange (Angayucham)

Table 2: List of geology (GEO) categories and corresponding names.

References

Abbott, B. W. and Jones, J. B. (2015) Permafrost collapse alters soil carbon stocks, respiration, CH4, and N2O in upland tundra. Global Change Biology **21**(12), 4570–4587.

Abedi, R., Costache, R., Shafizadeh-Moghadam, H. and Pham, Q. B. (2021) Flash-flood susceptibility mapping based on XGBoost, random forest and boosted regression trees. Geocarto International pp. 1–18.

Aguilera, Q., Lombardo, L., Tanyas, H. and Lipani, A. (2022) On the prediction of landslide occurrences and sizes via Hierarchical Neural Networks. Stochastic Environmental Research and Risk Assessment **36**(8), 2031–2048.

Alin, A. (2010) Multicollinearity. Wiley interdisciplinary reviews: computational statistics **2**(3), 370–374.

Amato, G., Eisank, C., Castro-Camilo, D. and Lombardo, L. (2019) Accounting for covariate distributions in slope-unit-based landslide susceptibility models. a case study in the alpine environment. Engineering Geology **260**, In print.

Amato, G., Fiorucci, M., Martino, S., Lombardo, L. and Palombi, L. (2021) Earthquake-triggered landslide susceptibility in Italy by means of Artificial Neural Network .

Amatya, P., Kirschbaum, D., Stanley, T. and Tanyas, H. (2021) Landslide mapping using object-based image analysis and open source tools. Engineering Geology **282**, 106000.

Anderson-Bell, J., Schillaci, C. and Lipani, A. (2021) Predicting non-residential building fire risk using geospatial information and convolutional neural networks. Remote Sensing Applications: Society and Environment **21**, 100470.

Atkinson, P. M. and Massari, R. (1998) Generalised linear modelling of susceptibility to landsliding in the central Apennines, Italy. Computers & Geosciences **24**(4), 373–385.

Avolio, M. V., Di Gregorio, S., Lupiano, V. and Mazzanti, P. (2013) Sciddica-ss 3: A new version of cellular automata model for simulating fast moving landslides. The Journal of Supercomputing **65**, 682–696.

Balser, A. W., Jones, J. B. and Gens, R. (2014) Timing of retrogressive thaw slump initiation in the Noatak Basin, northwest Alaska, USA. Journal of Geophysical Research: Earth Surface **119**(5), 1106–1120.

Beguería, S. (2006) Changes in land cover and shallow landslide activity: a case study in the spanish pyrenees. Geomorphology **74**(1-4), 196–206.

Behnia, P. and Blais-Stevens, A. (2018) Landslide susceptibility modelling using the quantitative random forest method along the northern portion of the Yukon Alaska Highway Corridor, Canada. Natural hazards **90**(3), 1407–1426.

Bertolini, R. (2021) Evaluating performance variability of data pipelines for binary classification with applications to predictive learning analytics. Ph.D. thesis, State University of New York at Stony Brook.

Bertrand, M., Liébault, F. and Piégay, H. (2013) Debris-flow susceptibility of upland catchments. Natural Hazards **67**, 497–511.

Bhuyan, K., Tanyaş, H., Nava, L., Puliero, S., Meena, S. R., Floris, M., van Westen, C. and Catani, F. (2023) Generating multi-temporal landslide inventories through a general deep transfer learning strategy using HR EO data. Scientific Reports **13**(1), 162.

Blais-Stevens, A., Kremer, M., Bonnaventure, P. P., Smith, S. L., Lipovsky, P. and Lewkowicz, A. G. (2014) 86 Active Layer Detachment Slides and Retrogressive Thaw Slumps Susceptibility Mapping for Current and Future Permafrost Distribution, Yukon Alaska Highway Corridor. Engineering Geology for Society and Territory-Volume 1: Climate Change and Engineering Geology p. 449.

Blais-Stevens, A., Kremer, M., Bonnaventure, P. P., Smith, S. L., Lipovsky, P. and Lewkowicz, A. G. (2015) Active layer detachment slides and retrogressive thaw slumps susceptibility mapping for current and future permafrost distribution, Yukon Alaska Highway Corridor. In Engineering Geology for Society and Territory-Volume 1: Climate Change and Engineering Geology, pp. 449–453.

Borrelli, P., Ballabio, C., Panagos, P. and Montanarella, L. (2014) Wind erosion susceptibility of European soils. Geoderma **232**, 471–478.

Borrelli, P., Panagos, P., Ballabio, C., Lugato, E., Weynants, M. and Montanarella, L. (2016) Towards a pan-European assessment of land susceptibility to wind erosion. Land Degradation & Development **27**(4), 1093–1105.

Boyd, D. W. (1976) Normal freezing and thawing degree-days from normal monthly temperatures. Canadian Geotechnical Journal **13**(2), 176–180.

Boyd, K., Eng, K. H. and Page, C. D. (2013) Area under the precision-recall curve: point estimates and confidence intervals. In Machine Learning and Knowledge Discovery in Databases: European Conference, ECML PKDD 2013, Prague, Czech Republic, September 23-27, 2013, Proceedings, Part III 13, pp. 451–466.

Brabb, E., Pampeyan, H. and Bonilla, M. (1972) MG 1972. landslide susceptibility in San Mateo County, California. US Geological Survey Miscellaneous Field Studies Map MF-360, scale **1**(62,500).

Brenning, A. (2008) Statistical geocomputing combining R and SAGA: The example of landslide susceptibility analysis with generalized additive models. Hamburger Beiträge zur Physischen Geographie und Landschaftsökologie **19**(23-32), 410.

Brenning, A. (2012) Spatial cross-validation and bootstrap for the assessment of prediction rules in remote sensing: The r package sperrorest. In 2012 IEEE international geoscience and remote sensing symposium, pp. 5372–5375.

Bryce, E., Lombardo, L., van Westen, C., Tanyas, H. and Castro-Camilo, D. (2022) Unified landslide hazard assessment using hurdle models: a case study in the island of dominica. Stochastic Environmental Research and Risk Assessment **36**(8), 2071–2084.

Cama, M., Lombardo, L., Conoscenti, C. and Rotigliano, E. (2017) Improving transferability strategies for debris flow susceptibility assessment: Application to the Saponara and Itala catchments (Messina, Italy). Geomorphology **288**, 52–65.

Cama, M., Schillaci, C., Kropáček, J., Hochschild, V., Bosino, A. and Märker, M. (2020) A probabilistic assessment of soil erosion susceptibility in a head catchment of the Jemma Basin, Ethiopian Highlands. Geosciences **10**(7), 248.

Carrara, A., Cardinali, M., Detti, R., Guzzetti, F., Pasqui, V. and Reichenbach, P. (1991) GIS techniques and statistical models in evaluating landslide hazard. Earth Surface Processes and Landforms **16**(5), 427–445.

Cassidy, A. E., Christen, A. and Henry, G. H. (2017) Impacts of active retrogressive thaw slumps on vegetation, soil, and net ecosystem exchange of carbon dioxide in the Canadian High Arctic. Arctic Science **3**(2), 179–202.

Castro Camilo, D., Lombardo, L., Mai, P., Dou, J. and Huser, R. (2017) Handling high predictor dimensionality in slope-unit-based landslide susceptibility models through LASSO-penalized Generalized Linear Model. Environmental Modelling and Software **97**, 145–156.

Chapin III, F. S. (1993) Functional role of growth forms in ecosystem and global processes. In Scaling physiological processes, pp. 287–312. Elsevier.

Chen, J., Yang, S., Li, H., Zhang, B. and Lv, J. (2013) Research on geographical environment unit division based on the method of natural breaks (Jenks). Int. Arch. Photogramm. Remote Sens. Spat. Inf. Sci **3**, 47–50.

Chen, W., Lei, X., Chakrabortty, R., Pal, S. C., Sahana, M. and Janizadeh, S. (2021) Evaluation of different boosting ensemble machine learning models and novel deep learning and boosting framework for head-cut gully erosion susceptibility. Journal of Environmental Management **284**, 112015.

Choubin, B., Moradi, E., Golshan, M., Adamowski, J., Sajedi-Hosseini, F. and Mosavi, A. (2019) An ensemble prediction of flood susceptibility using multivariate discriminant analysis, classification and regression trees, and support vector machines. Science of the Total Environment **651**, 2087–2096.

Conforti, M., Aucelli, P. P., Robustelli, G. and Scarciglia, F. (2011) Geomorphology and GIS analysis for mapping gully erosion susceptibility in the Turbolo stream catchment (Northern Calabria, Italy). Natural hazards **56**(3), 881–898.

Crisci, G. M., Rongo, R., Di Gregorio, S. and Spataro, W. (2004) The simulation model SCIARA: the 1991 and 2001 lava flows at Mount Etna. Journal of Volcanology and Geothermal Research **132**(2-3), 253–267.

Crosby, B. (2009) Progressive growth, modulated supply: how coupling and decoupling between an enormous retrogressive thaw slump and its depositional fan impacts sediment delivery to the selawik river, northwest alaska. In AGU Fall Meeting Abstracts, volume 2009, pp. U41C–0043.

Danielson, J. J. and Gesch, D. B. (2011) Global multi-resolution terrain elevation data 2010 (gmted2010) .

Deng, L., Smith, A., Dixon, N. and Yuan, H. (2021) Machine learning prediction of landslide deformation behaviour using acoustic emission and rainfall measurements. Engineering Geology **293**, 106315.

Dillon, J. T., Brosgé, W. P. and Dutro Jr, J. (1986) Generalized geologic map of the Wiseman quadrangle, Alaska. Technical report.

Ding, Y., Mu, C., Wu, T., Hu, G., Zou, D., Wang, D., Li, W. and Wu, X. (2021) Increasing cryospheric hazards in a warming climate. Earth-Science Reviews **213**, 103500.

Dobinski, W. (2011) Permafrost. Earth-Science Reviews **108**(3-4), 158–169.

Fang, Z., Wang, Y., Peng, L. and Hong, H. (2021) Predicting flood susceptibility using éLSTM neural networks. Journal of Hydrology **594**, 125734.

Fluss, R., Faraggi, D. and Reiser, B. (2005) Estimation of the Youden Index and its associated cutoff point. Biometrical Journal: Journal of Mathematical Methods in Biosciences **47**(4), 458–472.

Frattini, P., Crosta, G. and Carrara, A. (2010) Techniques for evaluating the performance of landslide susceptibility models. Engineering Geology **111**(1), 62–72.

Ghosh, A. and Maiti, R. (2021) Soil erosion susceptibility assessment using logistic regression, decision tree and random forest: study on the Mayurakshi river basin of Eastern India. Environmental Earth Sciences **80**(8), 1–16.

Goetz, J., Brenning, A., Petschko, H. and Leopold, P. (2015) Evaluating machine learning and statistical prediction techniques for landslide susceptibility modeling. Computers & geosciences **81**, 1–11.

Goetz, J. N., Guthrie, R. H. and Brenning, A. (2011) Integrating physical and empirical landslide susceptibility models using generalized additive models. Geomorphology **129**(3-4), 376–386.

Günther, A., Reichenbach, P., Malet, J.-P., Van Den Eeckhaut, M., Hervás, J., Dashwood, C. and Guzzetti, F. (2013) Tier-based approaches for landslide susceptibility assessment in Europe. Landslides **10**, 529–546.

Guzzetti, F., Mondini, A. C., Cardinali, M., Fiorucci, F., Santangelo, M. and Chang, K.-T. (2012) Landslide inventory maps: New tools for an old problem. Earth-Science Reviews **112**(1-2), 42–66.

Hajian-Tilaki, K. (2013) Receiver operating characteristic (roc) curve analysis for medical diagnostic test evaluation. Caspian journal of internal medicine **4**(2), 627.

Hall, D., Riggs, G. and Salomonson, V. (2016) Modis/terra snow cover daily l3 global 500m grid, version 6. Boulder, CO: NASA National Snow and Ice Data Center Distributed Active Archive Center .

Hastie, T. and Hastie, M. T. (2015) Package 'gam'. R package version pp. 90124–3.

Hastie, T. J. (2017) Generalized additive models. In Statistical models in S, pp. 249–307. Routledge.

Heerdegen, R. G. and Beran, M. A. (1982) Quantifying source areas through land surface curvature and shape. Journal of Hydrology **57**(3-4), 359–373.

Hjort, J., Streletskiy, D., Doré, G., Wu, Q., Bjella, K. and Luoto, M. (2022) Impacts of permafrost degradation on infrastructure. Nature Reviews Earth & Environment **3**(1), 24–38.

Hosmer, D. W. and Lemeshow, S. (2000) Applied Logistic Regression. Second edition. New York: Wiley.

Hu, S. (2007) Akaike information criterion. Center for Research in Scientific Computation **93**, 42.

Huang, L., Liu, L., Luo, J., Lin, Z. and Niu, F. (2021) Automatically quantifying evolution of retrogressive thaw slumps in Beiluhe (Tibetan Plateau) from multi-temporal CubeSat images. International Journal of Applied Earth Observation and Geoinformation **102**, 102399.

Huang, L., Luo, J., Lin, Z., Niu, F. and Liu, L. (2020) Using deep learning to map retrogressive thaw slumps in the Beiluhe region (Tibetan Plateau) from CubeSat images. Remote Sensing of Environment **237**, 111534.

Jafarov, E. E., Marchenko, S. S. and Romanovsky, V. (2012) Numerical modeling of permafrost dynamics in Alaska using a high spatial resolution dataset. The Cryosphere **6**(3), 613–624.

James, T., Schillaci, C. and Lipani, A. (2021) Convolutional neural networks for water segmentation using sentinel-2 red, green, blue (RGB) composites and derived spectral indices. International Journal of Remote Sensing **42**(14), 5338–5365.

Jenks, G. F. (1967) The data model concept in statistical mapping. International yearbook of cartography **7**, 186–190.

Jones, M. K. W., Pollard, W. H. and Jones, B. M. (2019) Rapid initialization of retrogressive thaw slumps in the Canadian high Arctic and their response to climate and terrain factors. Environmental Research Letters **14**(5), 055006.

Jorgenson, M. T., Racine, C. H., Walters, J. C. and Osterkamp, T. E. (2001) Permafrost degradation and ecological changes associated with a warmingclimate in central Alaska. Climatic change **48**(4), 551–579.

Jorgenson, M. T., Shur, Y. L. and Pullman, E. R. (2006) Abrupt increase in permafrost degradation in Arctic Alaska. Geophysical Research Letters **33**(2).

Juliev, M., Mergili, M., Mondal, I., Nurtaev, B., Pulatov, A. and Hübl, J. (2019) Comparative analysis of statistical methods for landslide susceptibility mapping in the Bostanlik District, Uzbekistan. Science of the total environment **653**, 801–814.

Kearney, S. P., Coops, N. C., Sethi, S. and Stenhouse, G. B. (2020) Maintaining accurate, current, rural road network data: An extraction and updating routine using RapidEye, participatory GIS and deep learning. International Journal of Applied Earth Observation and Geoinformation **87**, 102031.

Khan, J. A., Van Aelst, S. and Zamar, R. H. (2007) Building a robust linear model with forward selection and stepwise procedures. Computational Statistics & Data Analysis **52**(1), 239–248.

Khosravi, K., Pham, B. T., Chapi, K., Shirzadi, A., Shahabi, H., Revhaug, I., Prakash, I. and Bui, D. T. (2018) A comparative assessment of decision trees algorithms for flash flood susceptibility modeling at Haraz watershed, northern Iran. Science of the Total Environment **627**, 744–755.

Klapstein, S. J., Turetsky, M. R., McGuire, A. D., Harden, J. W., Czimczik, C. I., Xu, X., Chanton, J. P. and Waddington, J. M. (2014) Controls on methane released through ebullition in peatlands affected by permafrost degradation. Journal of Geophysical Research: Biogeosciences **119**(3), 418–431.

Knoblauch, C., Beer, C., Sosnin, A., Wagner, D. and Pfeiffer, E.-M. (2013) Predicting long-term carbon mineralization and trace gas production from thawing permafrost of n ortheast s iberia. Global change biology **19**(4), 1160–1172.

Kokelj, S. V. and Jorgenson, M. (2013) Advances in thermokarst research. Permafrost and Periglacial Processes **24**(2), 108–119.

Kokelj, S. V., Lantz, T. C., Kanigan, J., Smith, S. and Coutts, R. (2009) Origin and polycyclic behaviour of tundra thaw slumps, Mackenzie Delta region, Northwest Territories, Canada. Permafrost and Periglacial Processes **20**(2), 173–184.

Kokelj, S. V., Tunnicliffe, J. F. and Lacelle, D. (2017) The peel plateau of northwestern canada: An ice-rich hummocky moraine landscape in transition. Landscapes and landforms of western Canada pp. 109–122.

Lacelle, D., Bjornson, J. and Lauriol, B. (2010) Climatic and geomorphic factors affecting contemporary (1950–2004) activity of retrogressive thaw slumps on the aklavik plateau, richardson mountains, nwt, canada. Permafrost and Periglacial Processes **21**(1), 1–15.

Lacelle, D., Brooker, A., Fraser, R. H. and Kokelj, S. V. (2015) Distribution and growth of thaw slumps in the Richardson Mountains–Peel Plateau region, northwestern Canada. Geomorphology **235**, 40–51.

Lamoureux, S. F. and Lafrenière, M. J. (2009) Fluvial impact of extensive active layer detachments, cape bounty, melville island, canada. Arctic, Antarctic, and Alpine Research **41**(1), 59–68.

Lantz, T. C. and Kokelj, S. V. (2008) Increasing rates of retrogressive thaw slump activity in the Mackenzie Delta region, NWT, Canada. Geophysical Research Letters **35**(6).

Leoni, G., Barchiesi, F., Catallo, F., Dramis, F., Fubelli, G., Lucifora, S., Mattei, M., Pezzo, G. and Puglisi, C. (2009) GIS methodology to assess landslide susceptibility: application to a river catchment of Central Italy. Journal of maps **5**(1), 87–93.

Leuenberger, M., Parente, J., Tonini, M., Pereira, M. G. and Kanevski, M. (2018) Wildfire susceptibility mapping: Deterministic vs. stochastic approaches. Environmental Modelling & Software **101**, 194–203.

Lewkowicz, A. G. (2007) Dynamics of active-layer detachment failures, fosheim peninsula, ellesmere island, nunavut, canada. Permafrost and Periglacial Processes **18**(1), 89–103.

Li, H., Zhang, G., Wang, C., Liu, Z., Ju, C. and Mamtimin, A. (2023) Improving snow albedo parameterization scheme based on remote sensing data. Atmospheric Research p. 106602.

Liljedahl, A. K., Boike, J., Daanen, R. P., Fedorov, A. N., Frost, G. V., Grosse, G., Hinzman, L. D., Iijma, Y., Jorgenson, J. C., Matveyeva, N. et al. (2016) Pan-arctic ice-wedge degradation in warming permafrost and its influence on tundra hydrology. Nature Geoscience **9**(4), 312–318.

Lima, P., Steger, S. and Glade, T. (2021) Counteracting flawed landslide data in statistically based landslide susceptibility modelling for very large areas: a national-scale assessment for austria. Landslides **18**(11), 3531–3546.

Ling, F. and Zhang, T. (2003) Numerical simulation of permafrost thermal regime and talik development under shallow thaw lakes on the Alaskan Arctic Coastal Plain. Journal of Geophysical Research: Atmospheres **108**(D16).

Liong, S.-Y. and Sivapragasam, C. (2002) Flood stage forecasting with support vector machines 1. JAWRA Journal of the American Water Resources Association **38**(1), 173–186.

Loche, M., Scaringi, G., Yunus, A. P., Catani, F., Tanyaş, H., Frodella, W., Fan, X. and Lombardo, L. (2022) Surface temperature controls the pattern of post-earthquake landslide activity. Scientific reports **12**(1), 988.

Lombardo, L. and Mai, P. M. (2018) Presenting logistic regression-based landslide susceptibility results. Engineering geology **244**, 14–24.

Lombardo, L. and Tanyas, H. (2020) Chrono-validation of near-real-time landslide susceptibility models via plug-in statistical simulations. Engineering Geology **278**, 105818.

Lombardo, L., Tanyas, H., Huser, R., Guzzetti, F. and Castro-Camilo, D. (2021) Landslide size matters: A new data-driven, spatial prototype. Engineering Geology **293**, 106288.

Lombardo, L., Tanyas, H. and Nicu, I. C. (2020) Spatial modeling of multi-hazard threat to cultural heritage sites. Engineering Geology p. 105776.

Longley, P. A., Goodchild, M. F., Maguire, D. J. and Rhind, D. W. (2005) Geographic information systems and science. John Wiley & Sons.

Mende, T. and Koschke, R. (2010) Effort-aware defect prediction models. In 2010 14th European Conference on Software Maintenance and Reengineering, pp. 107–116.

Meusburger, K. and Alewell, C. (2009) On the influence of temporal change on the validity of landslide susceptibility maps. Natural Hazards and Earth System Sciences **9**(4), 1495–1507.

Nicu, I. C., Elia, L., Rubensdotter, L., Tanyaş, H. and Lombardo, L. (2023) Multi-hazard susceptibility mapping of cryospheric hazards in a high-Arctic environment: Svalbard Archipelago. Earth System Science Data **15**(1), 447–464.

Nicu, I. C. and Fatorić, S. (2023) Climate change impacts on immovable cultural heritage in polar regions: A systematic bibliometric review. Wiley Interdisciplinary Reviews: Climate Change p. e822.

Nicu, I. C., Lombardo, L. and Rubensdotter, L. (2021) Preliminary assessment of thaw slump hazard to arctic cultural heritage in nordenskiöld land, svalbard. Landslides **18**(8), 2935–2947.

Nicu, I. C., Stalsberg, K., Rubensdotter, L., Martens, V. V. and Flyen, A.-C. (2020) Coastal erosion affecting cultural heritage in svalbard. a case study in hiorthhamn (adventfjorden)—an abandoned mining settlement. Sustainability **12**(6), 2306.

Nitze, I., Heidler, K., Barth, S. and Grosse, G. (2021) Developing and testing a deep learning approach for mapping retrogressive thaw slumps. Remote Sensing **13**(21), 4294.

Ohlmacher, G. C. (2007) Plan curvature and landslide probability in regions dominated by earth flows and earth slides. Engineering Geology **91**(2), 117–134.

Osterkamp, T. (2005) The recent warming of permafrost in Alaska. Global and Planetary Change **49**(3-4), 187–202.

Osterkamp, T. and Romanovsky, V. (1999) Evidence for warming and thawing of discontinuous permafrost in Alaska. Permafrost and periglacial Processes **10**(1), 17–37.

Peel, M. C., Finlayson, B. L. and McMahon, T. A. (2007) Updated world map of the Köppen-Geiger climate classification. Hydrology and earth system sciences **11**(5), 1633–1644.

Petschko, H., Bell, R., Brenning, A. and Glade, T. (2012) Landslide susceptibility modeling with generalized additive models–facing the heterogeneity of large regions. Landslides and Engineered Slopes, Protecting Society through Improved Understanding **1**, 769–777.

Quesada-Román, A., Fallas-López, B., Hernández-Espinoza, K., Stoffel, M. and Ballesteros-Cánovas, J. A. (2019) Relationships between earthquakes, hurricanes, and landslides in Costa Rica. Landslides **16**(8), 1539–1550.

Rahmati, O., Kornejady, A., Samadi, M., Deo, R. C., Conoscenti, C., Lombardo, L., Dayal, K., Taghizadeh-Mehrjardi, R., Pourghasemi, H. R., Kumar, S. et al. (2019) PMT: New analytical framework for automated evaluation of geo-environmental modelling approaches. Science of the total environment **664**, 296–311.

Ramage, J. L., Irrgang, A. M., Herzschuh, U., Morgenstern, A., Couture, N. and Lantuit, H. (2017) Terrain controls on the occurrence of coastal retrogressive thaw slumps along the Yukon Coast, Canada. Journal of Geophysical Research: Earth Surface **122**(9), 1619–1634.

Randall, D. o., Cess, R., Blanchet, J., Chalita, S., Colman, R., Dazlich, D., Del Genio, A., Keup, E., Lacis, A., Le Treut, H. et al. (1994) Analysis of snow feedbacks in 14 general circulation models. Journal of Geophysical Research: Atmospheres **99**(D10), 20757–20771.

Rantanen, M., Karpechko, A. Y., Lipponen, A., Nordling, K., Hyvärinen, O., Ruosteenoja, K., Vihma, T. and Laaksonen, A. (2022) The arctic has warmed nearly four times faster than the globe since 1979. Communications Earth & Environment **3**(1), 1–10.

Regmi, N. R., Giardino, J. R. and Vitek, J. D. (2010) Modeling susceptibility to landslides using the weight of evidence approach: Western Colorado, USA. Geomorphology **115**(1-2), 172–187.

Reichenbach, P., Rossi, M., Malamud, B. D., Mihir, M. and Guzzetti, F. (2018) A review of statistically-based landslide susceptibility models. Earth-Science Reviews **180**, 60–91.

Roberts, D. R., Bahn, V., Ciuti, S., Boyce, M. S., Elith, J., Guillera-Arroita, G., Hauenstein, S., Lahoz-Monfort, J. J., Schröder, B., Thuiller, W. et al. (2017) Cross-validation strategies for data with temporal, spatial, hierarchical, or phylogenetic structure. Ecography **40**(8), 913–929.

Rouse, J. W., Haas, R. H., Schell, J. A., Deering, D. W. et al. (1974) Monitoring vegetation systems in the Great Plains with ERTS. NASA Spec. Publ **351**(1), 309.

Rudy, A. C., Lamoureux, S. F., Treitz, P. and Collingwood, A. (2013) Identifying permafrost slope disturbance using multi-temporal optical satellite images and change detection techniques. Cold Regions Science and Technology **88**, 37–49.

Rudy, A. C., Lamoureux, S. F., Treitz, P. and Van Ewijk, K. Y. (2016) Transferability of regional permafrost disturbance susceptibility modelling using generalized linear and generalized additive models. Geomorphology **264**, 95–108.

Sattler, K., Keiler, M., Zischg, A. and Schrott, L. (2011) On the connection between debris flow activity and permafrost degradation: a case study from the schnalstal, south tyrolean alps, italy. Permafrost and Periglacial Processes **22**(3), 254–265.

Servén, D. and Brummitt, C. (2018) pygam: Generalized additive models in python. Zenodo. doi **10**.

Servén, D. and Brummitt, C. (2018) pygam: Generalized additive models in python.

Shiklomanov, N. I., Streletskiy, D. A., Nelson, F. E., Hollister, R. D., Romanovsky, V. E., Tweedie, C. E., Bockheim, J. G. and Brown, J. (2010) Decadal variations of active-layer thickness in moisture-controlled landscapes, barrow, alaska. Journal of Geophysical Research: Biogeosciences **115**(G4).

Stafford, J., Wendler, G. and Curtis, J. (2000) Temperature and precipitation of Alaska: 50 year trend analysis. Theoretical and Applied Climatology **67**, 33–44.

Stanley, T. and Kirschbaum, D. B. (2017) A heuristic approach to global landslide susceptibility mapping. Natural hazards **87**, 145–164.

Steger, S., Mair, V., Kofler, C., Pittore, M., Zebisch, M. and Schneiderbauer, S. (2021a) Correlation does not imply geomorphic causation in data-driven landslide susceptibility modelling–Benefits of exploring landslide data collection effects. Science of the total environment **776**, 145935.

Steger, S., Mair, V., Kofler, C., Pittore, M., Zebisch, M. and Schneiderbauer, S. (2021b) Correlation does not imply geomorphic causation in data-driven landslide susceptibility modelling–benefits of exploring landslide data collection effects. Science of the total environment **776**, 145935.

Steger, S., Scorpio, V., Comiti, F. and Cavalli, M. (2022) Data-driven modelling of joint debris flow release susceptibility and connectivity. Earth Surface Processes and Landforms **47**(11), 2740–2764.

Streletskiy, D., Anisimov, O. and Vasiliev, A. (2015) Permafrost degradation. In Snow and ice-related hazards, risks, and disasters, pp. 303–344. Elsevier.

Swanson, D. K. (2021) Permafrost thaw-related slope failures in alaska's arctic national parks, c. 1980–2019. Permafrost and periglacial processes **32**(3), 392–406.

Swanson, D. K. and Nolan, M. (2018) Growth of retrogressive thaw slumps in the Noatak Valley, Alaska, 2010–2016, measured by airborne photogrammetry. Remote Sensing **10**(7), 983.

Tailleur, I., Brosge, W. and Reiser, H. (1967) Palinspastic analysis of devonian rocks in northwestern alaska .

Tananaev, N. and Lotsari, E. (2022) Defrosting northern catchments: Fluvial effects of permafrost degradation. Earth-Science Reviews **228**, 103996.

Tanyaş, H., Rossi, M., Alvioli, M., van Westen, C. J. and Marchesini, I. (2019) A global slope unit-based method for the near real-time prediction of earthquake-induced landslides. Geomorphology **327**, 126–146.

Thornton, P., Thornton, M., Mayer, B., Wilhelmi, N., Wei, Y., Devarakonda, R. and Cook, R. (2014) Daymet: Daily surface weather data on a 1-km grid for north america, version 2. data set. Available on-line [http://daac. ornl. gov] from Oak Ridge National Laboratory Distributed Active Archive Center, Oak Ridge, Tennessee, USA. Date accessed: 2014/08/13. Temporal range: 2000/01/01-2013/12 **31**.

Titti, G., Napoli, G. N., Conoscenti, C. and Lombardo, L. (2022a) Cloud-based interactive susceptibility modeling of gully erosion in Google Earth Engine. International Journal of Applied Earth Observation and Geoinformation **115**, 103089.

Titti, G., Sarretta, A., Lombardo, L., Crema, S., Pasuto, A. and Borgatti, L. (2022b) Mappin g susceptibility with open-source tools: a new plugin for QGIS. Front. Earth Sci **229**.

Titti, G., van Westen, C., Borgatti, L., Pasuto, A. and Lombardo, L. (2021) When enough is really enough? on the minimum number of landslides to build reliable susceptibility models. Geosciences **11**(11), 469.

Turetsky, M. R., Abbott, B. W., Jones, M. C., Anthony, K. W., Olefeldt, D., Schuur, E. A., Grosse, G., Kuhry, P., Hugelius, G., Koven, C. et al. (2020) Carbon release through abrupt permafrost thaw. Nature Geoscience **13**(2), 138–143.

Verstappen, H. T. (1983) Applied geomorphology: geomorphological surveys for environmental development. Number 551.4 VER.

Wan, Z. (2015) University of california santa barbara, simon hook, glynn hulley-jpl and modaps sips-nasa. MOD11A1 MODIS/Terra Land Surface Temperature and the Emissivity Daily L3 Global 1km SIN Grid. NASA LP DAAC .

Wang, N., Cheng, W., Marconcini, M., Bachofer, F., Liu, C., Xiong, J. and Lombardo, L. (2022a) Space-time susceptibility modeling of hydro-morphological processes at the Chinese national scale. Engineering geology **301**, 106586.

Wang, Z., Goetz, J. and Brenning, A. (2022b) Transfer learning for landslide susceptibility modeling using domain adaptation and case-based reasoning. Geoscientific Model Development **15**(23), 8765–8784.

Wendler, G., Gordon, T. and Stuefer, M. (2017) On the precipitation and precipitation change in Alaska. Atmosphere **8**(12), 253.

Wilson, F. H. and Labay, K. A. (2016) Alaska geology revealed. Technical report, US Geological Survey.

Witharana, C., Udawalpola, M. R., Liljedahl, A. K., Jones, M. K. W., Jones, B. M., Hasan, A., Joshi, D. and Manos, E. (2022) Automated Detection of Retrogressive Thaw Slumps in the High Arctic Using High-Resolution Satellite Imagery. Remote Sensing **14**(17), 4132.

Wood, S. N. (2006) *Generalized additive models: an introduction with R*. chapman and hall/CRC.

Wood, S. N. (2017) *Generalized additive models: an introduction with R*. CRC press.

Yalcin, A., Reis, S., Aydinoglu, A. and Yomralioglu, T. (2011) A gis-based comparative study of frequency ratio, analytical hierarchy process, bivariate statistics and logistics regression methods for landslide susceptibility mapping in trabzon, ne turkey. *Catena* **85**(3), 274–287.

Yang, Y., Rogers, B. M., Fiske, G., Watts, J., Potter, S., Windholz, T., Mullen, A., Nitze, I. and Natali, S. M. (2023) Mapping retrogressive thaw slumps using deep neural networks. *Remote Sensing of Environment* **288**, 113495.

Zevenbergen, L. W. and Thorne, C. R. (1987) Quantitative analysis of land surface topography. *Earth surface processes and landforms* **12**(1), 47–56.

Zheng, L., Overeem, I., Wang, K. and Clow, G. D. (2019) Changing arctic river dynamics cause localized permafrost thaw. *Journal of Geophysical Research: Earth Surface* **124**(9), 2324–2344.